Tetranuclear Manganese Carboxylate Complexes with a Trigonal Pyramidal Metal Topology via Controlled Potential Electrolysis

Sheyi Wang,[1a] Michael S. Wemple,[1a] Jae Yoo,[1c] Kirsten Folting,[1a] John C. Huffman,[1a] Karl S. Hagen,[1b] David N. Hendrickson,*[,1c] and George Christou*[,1a]

Department of Chemistry and Molecular Structure Center, Indiana University, Bloomington, Indiana 47405-7102, Department of Chemistry, Emory University, Atlanta, Georgia 30322, and Department of Chemistry−0358, University of California at San Diego, La Jolla, California 92093-0358

Received September 7, 1999

Controlled potential electrolysis (CPE) procedures are described that provide access to complexes with a $[Mn_4(\mu_3\text{-}O)_3(\mu_3\text{-}O_2CR)]^{6+}$ core ($3Mn^{III},Mn^{IV}$) and a trigonal pyramidal metal topology, starting from species containing the $[Mn_4(\mu_3\text{-}O)_2]^{8+}$ core ($4Mn^{III}$). $[Mn_4O_2(O_2CMe)_6(py)_2(dbm)_2]$ (**6**): triclinic, $P\bar{1}$, $a = 10.868(3)$ Å, $b = 13.864(3)$ Å, $c = 10.625(3)$ Å, $\alpha = 108.62(1)°$, $\beta = 118.98(1)°$, $\gamma = 89.34(2)°$, $V = 1307$ Å^3, $Z = 1$, $T = -131$ °C, R (R_w) = 3.24 (3.70)%. $[Mn_4O_2(O_2CPh)_6(py)(dbm)_2]$ (**8**): monoclinic, $P2_1/c$, $a = 14.743(6)$ Å, $b = 15.536(8)$ Å, $c = 30.006(13)$ Å, $\beta = 102.79(1)°$, $V = 6702$ Å^3, $Z = 4$, $T = -155$ °C, R (R_w) = 4.32 (4.44)%. Both **6** and **8** contain a $[Mn_4O_2]^{8+}$ core; **8** only has one py group, the fourth Mn^{III} site being five-coordinate. $(NBu^n_4)[Mn_4O_2(O_2CPh)_7(dbm)_2]$ (**10**) is available from two related procedures. CPE of **10** at 0.65 V vs ferrocene in MeCN leads to precipitation of $[Mn_4O_3(O_2CPh)_4(dbm)_3]$ (**11**); similarly, CPE of **6** at 0.84 V in $MeCN/CH_2Cl_2$ (3:1 v/v) gives $[Mn_4O_3(O_2CMe)_4(dbm)_3]$ (**12**). Complex **11**: monoclinic, $P2_1/n$, $a = 15.161(3)$ Å, $b = 21.577(4)$ Å, $c = 22.683(5)$ Å, $\beta = 108.04(3)°$, $V = 7056$ Å^3, $Z = 4$, $T = -100$ °C, R (wR2) = 8.63 (21.80)%. Complex **12**: monoclinic, $P2_1/n$, $a = 13.549(2)$ Å, $b = 22.338(4)$ Å, $c = 16.618(2)$ Å, $\beta = 103.74(1)°$, $V = 4885$ Å^3, $Z = 4$, $T = -171$ °C, R (R_w) = 4.63 (4.45)%. Both **11** and **12** contain a $[Mn_4(\mu_3\text{-}O)_3(\mu\text{-}O_2CR)]$ core with a Mn_4 trigonal pyramid (Mn^{IV} at the apex) and the RCO_2^- bridging the Mn^{III}_3 base. However, in **11**, the carboxylate is η^2,μ_3 with one O atom terminal to one Mn^{III} and the other O atom bridging the other two Mn^{III} ions, whereas in **12** the carboxylate is η^1,μ_3, a single O atom bridging three Mn^{III} ions. Variable-temperature, solid-state magnetic susceptibility studies on **11** and **12** show that, for both complexes, there are antiferromagnetic exchange interactions between Mn^{III}/Mn^{IV} pairs, and ferromagnetic interactions between Mn^{III}/Mn^{III} pairs. In both cases, the resultant ground state of the complex is $S = {}^9/_2$, confirmed by magnetization vs field studies in the 2.00−30.0 K and 0.50−50 kG temperature and field ranges, respectively.

Introduction

Manganese carboxylate cluster chemistry is of interest from a variety of viewpoints, including magnetic materials and bioinorganic chemistry. In the former area, it has been found that such clusters often possess large numbers of unpaired electrons,[2] making them attractive as potential precursors to molecule-based magnetic materials or as discrete, nanoscale magnetic particles in their own right.[2−5] In the bioinorganic arena, a tetranuclear Mn cluster is an integral component in the photosystem II reaction center of green plants, which is responsible for the light-driven oxidation of water to O_2 gas.[6−9] This Mn_4-containing water oxidation complex (WOC) is the site of water binding, deprotonation, and oxidative coupling to O_2, but the precise mechanism remains unestablished. EXAFS studies have shown that a minimal structural fragment of the WOC is a $[Mn_2(\mu\text{-}O)_2]$ unit with a Mn···Mn separation of ca. 2.7 Å, and it has been suggested that the WOC contains two such units in close proximity, although several structural possibilities for the complete Mn_4 unit still remain.[7] During function, the WOC cycles through five oxidation levels labeled S_0-S_4, the highest spontaneously reductively eliminating O_2 and returning to S_0.[6]

In the last 15 years or so, a variety of tetranuclear clusters have been synthesized as inorganic models of the WOC.[10−12] Most of these have some structural/spectroscopic/physical properties similar to those of the WOC, but no synthetic species

(1) (a) Indiana University. (b) University of California at San Diego. (c) Emory University.
(2) (a) Christou, G. In *Magnetism: A Supramolecular Function*: Kahn, O., Ed.; NATO ASI Series; Kluwer: Dordrecht, The Netherlands, 1996; pp 383−410. (b) Aromí, G.; Aubin, S. M. J.; Bolcar, M. A.; Christou, G.; Eppley, H. J.; Folting, K.; Hendrickson, D. N.; Huffman, J. C.; Squire, R. C.; Tsai, H.-L.; Wang, S.; Wemple, M. W. *Polyhedron* **1998**, *17*, 3005.
(3) (a) Sessoli, R.; Tsai, H.-L.; Schake, A. R.; Wang, S.; Vincent, J. B.; Folting, K.; Gatteschi, D.; Christou, G.; Hendrickson, D. N. *J. Am. Chem. Soc.* **1993**, *115*, 1804. (b) Sessoli, R.; Gatteschi, D.; Caneschi, A.; Novak, M. A. *Nature* **1993**, *365*, 141.
(4) (a) Aubin, S. M. J.; Dilley, N. R.; Wemple, M. W.; Maple, M. B.; Christou, G.; Hendrickson, D. N. *J. Am. Chem. Soc.* **1998**, *120*, 839. (b) Aubin, S. M. J.; Dilley, N. R.; Pardi, L.; Krzystek, J.; Wemple, M. W.; Brunel, L.-C.; Maple, M. B.; Christou, G.; Hendrickson, D. N. *J. Am. Chem. Soc.* **1998**, *120*, 4991. (c) Aubin, S. M. J.; Wemple, M. W.; Adams, D. M.; Tsai, H.-L.; Christou, G.; Hendrickson, D. N. *J. Am. Chem. Soc.* **1996**, *118*, 7746.
(5) Brechin, E. K.; Yoo, J.; Nakano, M.; Huffman, J. C.; Hendrickson, D. N.; Christou, G. *Chem. Commun.* **1999**, 783.
(6) (a) Debus, R. J. *Biochim. Biophys. Acta* **1992**, *1102*, 269 and references therein. (b) *Manganese Redox Enzymes*; Pecoraro, V. L., Ed.; Verlag Chemie: Weinheim, Germany, 1992. (c) Penner-Hahn, J. E. *Struct. Bonding* **1998**, *90*, 1.
(7) Yachandra, V. K.; Sauer, K.; Klein, M. P. *Chem. Rev.* **1996**, *96*, 2927.
(8) Ruttinger, W.; Dismukes, G. C. *Chem. Rev.* **1997**, *97*, 1.
(9) Tommos, C.; Babcock, G. T. *Acc. Chem. Res.* **1998**, *31*, 18.

10.1021/ic991068m CCC: $19.00
Published on Web 03/14/2000

currently seems to reproduce the properties of the WOC in all ways, and a satisfactory synthetic model of the WOC has thus yet to be obtained.

Although the mechanism of action of the WOC is uncertain, it is clear that the binding, deprotonation, and oxidation of substrate H_2O molecules are coupled to and driven by the sequentially increasing oxidation level of the WOC. For this reason, we have recently been exploring the oxidation reactions of certain synthetic Mn_4 complexes in our possession, seeking to identify the structural and reactivity consequences of oxidation, particularly in the presence of H_2O groups. Specifically, we have found that electrochemical oxidation of $[Mn_4O_2]^{8+}$-containing species such as $[Mn_4O_2(O_2CMe)_6(py)_2(dbm)_2]$ ($4Mn^{III}$; dbm^- is the anion of dibenzoylmethane) leads to a core transformation and a resultant increase in the O^{2-}:Mn ratio from 2:4 to 3:4, suggesting incorporation and deprotonation of a H_2O molecule.

In this paper are described the preparation and solid-state structural and magnetochemical properties of the products of two such oxidation products, both of formula $[Mn_4O_3(O_2CR)_4(dbm)_3]$. In subsequent papers will be reported their solution properties and site-specific ligand substitution reactions.[13]

Experimental Section

Syntheses. All manipulations were performed under aerobic conditions, using materials as received, except where noted otherwise. Where dried solvents were required, they were distilled from CaH_2 (MeCN) or Na/benzophenone (Et_2O, THF). The complexes $[Mn_3O(O_2CMe)_6(py)_3](ClO_4)$ (**1**),[14] $[Mn_3O(O_2CEt)_6(py)_3](ClO_4)$,[15] $[Mn_3O(O_2CPh)_6(py)_2(H_2O)]$ (**2**),[14] $(NBu^n_4)[Mn_4O_2(O_2CPh)_9(H_2O)]$,[16] and $(NBu^n_4)[Mn_4O_2(O_2CPh)_8(dbm)]$[16] were prepared as described previously. The syntheses below are summarized in Scheme 1: acacH = acetylacetone (pentane-2,4-dione); dbmH = dibenzoylmethane; picH = picolinic acid.

Scheme 1

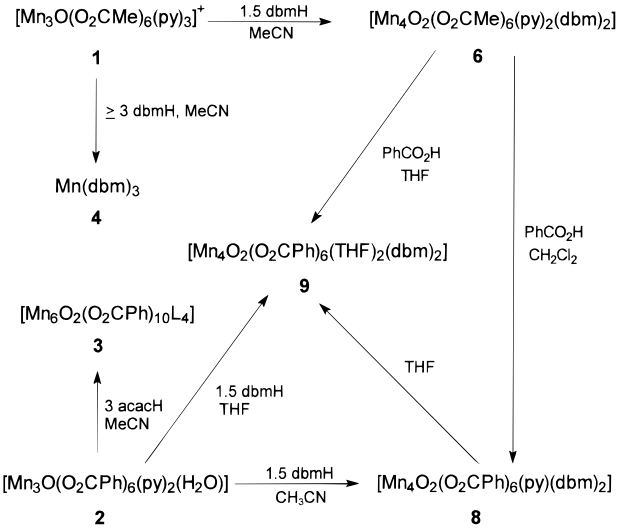

Na(dbm). A slurry of NaOH (1.06 g, 26.5 mmol) and dbmH (6.00 g, 26.8 mmol) in EtOH (45 mL) was stirred overnight to give a fine yellow precipitate. The solvent was removed in vacuo and the yellow solid washed with pentane (3 × 15 mL) to remove unreacted dbmH and dried in air. The yield was essentially quantitative. Anal. Calcd (found) for $C_{15}H_{11}O_2Na$: C, 73.16 (72.89); H, 4.50 (4.51); Na, 9.34 (9.38).

$[Mn_6O_2(O_2CPh)_{10}L_4]$ (3). To a stirred yellow-brown solution of $[Mn_3O(O_2CPh)_6(py)_3](ClO_4)$ (1.24 g, 1.00 mmol) in MeCN (30 mL) was added acacH (0.31 mL, 3.0 mmol) dropwise to give a deep brown solution. No immediate precipitate was observed, but slow formation of a fine orange-brown solid began soon after. When precipitation was judged complete (3 days), the orange-brown powder was collected by filtration, washed with MeCN, and dried in air. The complex was identified as $[Mn_6O_2(O_2CPh)_{10}(py)_2(MeCN)_2]$ (**3a**) by IR spectral comparison with authentic material. The yield was 45−60%. Use of complex **2** also gives **3a** in comparable yield.

Recrystallization of complex **3a** from a DMF solution that was carefully layered with a 1:1 (v/v) solution of Et_2O/hexanes slowly gave large brown crystals that were collected by filtration, washed with Et_2O, and dried in air. The complex was identified as $[Mn_6O_2(O_2CPh)_{10}(DMF)_4]\cdot C_6H_{14}$ (**3b**) by IR, elemental analysis, and crystallography. Anal. Calcd (found) for $C_{88}H_{92}N_4O_{26}Mn_6$: C, 54.16 (54.15); H, 4.75 (4.5); N, 2.87 (3.15); Mn, 16.89 (16.6).

$[Mn(dbm)_3]$ (4). To a stirred solution of complex **1**, $[Mn_3O(O_2CMe)_6(py)_3](ClO_4)$ (0.87 g, 1.0 mmol), in MeCN (25 mL) was added solid dbmH (0.70 g, 3.1 mmol) in small portions. A brown precipitate was rapidly formed. After several hours, the solid was collected by filtration, washed with MeCN, and dried in air. Recrystallization from CH_2Cl_2/hexanes, $CHCl_3$/hexanes, or THF/Et_2O gave well-formed black crystals. The yield varies depending on the ratio of complex **1**:dbmH used. For example, when the ratio was 1:3, the yield was 20%; with the ratio changed to 1:5, the yield was 53%. Anal. Calcd (found) for $C_{45}H_{33}O_6Mn$: C, 74.58 (74.8); H, 4.60 (4.6); Mn, 7.58 (7.6). Electronic spectrum: λ_{max}, nm (ϵ_M, L mol^{-1} cm^{-1}) in CH_2Cl_2: 368 (36 000), 284 (50 000).

$[Mn(dbm)_2(py)_2](ClO_4)$ (5). $Mn(ClO_4)_2\cdot 6H_2O$ (3.61 g, 10.0 mmol) and dbmH (5.94 g, 27.0 mmol) were dissolved in a solvent mixture comprising pyridine (15 mL) and EtOH (25 mL) to give an orange solution. To this solution was added solid $NBu^n_4MnO_4$ (1.26 g, 3.50 mmol) in small portions to give a green-brown solution and a brown crystalline precipitate. After several hours, the crystalline solid was

(10) (a) Wieghardt, K. *Angew. Chem., Int. Ed. Engl.* **1989**, *28*, 1153. (b) Pecoraro, V. L. *Photochem. Photobiol.* **1988**, *48*, 249. (c) Christou, G. *Acc. Chem. Res.* **1989**, *22*, 328. (d) Armstrong, W. H. In ref 6b, pp 261−286.

(11) (a) Philouze, C.; Blondin, G.; Girerd, J.-J.; Guilhem, J.; Pascard, C.; Lexa, D. *J. Am. Chem. Soc.* **1994**, *116*, 8557. (b) Chan, M. K.; Armstrong, W. H. *J. Am. Chem. Soc.* **1990**, *112*, 4985. (c) Chandra, S. K.; Chakraborty, P.; Chakravorty, A. *J. Chem. Soc., Dalton Trans.* **1993**, 863. (d) Sakiyama, H.; Tokuyama, K.; Matsumura, Y.; Okawa, H. *J. Chem. Soc., Dalton Trans.* **1993**, 2329. (e) Kirk, M. L.; Chan, M. K.; Armstrong, W. H.; Solomon, E. I. *J. Am. Chem. Soc.* **1992**, *114*, 10432. (f) Gedye, C.; Harding, C.; McKee, V.; Nelson, J.; Patterson, J. *J. Chem. Soc., Chem. Commun.* **1992**, 392. (g) Ruettinger, W. F.; Campana, C.; Dismukes, G. C. *J. Am. Chem. Soc.* **1997**, *119*, 6670. (h) Mikuriya, M.; Hashimoto, Y.; Kawamori, A. *Chem. Lett.* **1995**, 1095. (i) Kawasaki, H.; Kusunoki, M.; Hayashi, Y.; Suzuki, M.; Munezawa, K.; Suenaga, M.; Senda, H.; Uehara, A. *Bull. Chem. Soc. Jpn* **1994**, *67*, 1310. (j) McKee, V.; Tandon, S. S. *J. Chem. Soc., Chem. Commun.* **1988**, 1334. (k) Hagen, K. S.; Westmoreland, T. D.; Scott, M. J.; Armstrong, W. H. *J. Am. Chem. Soc.* **1989**, *111*, 1907. (l) Dubé, C. E.; Wright, D. W.; Pal, S.; Bonitatebus, P. J.; Armstrong, W. H. *J. Am. Chem. Soc.* **1998**, *120*, 3704.

(12) (a) Wang, S.; Tsai, H.-L.; Libby, E.; Folting, K.; Streib, W. E.; Hendrickson, D. N.; Christou, G. *Inorg. Chem.* **1996**, *35*, 7578. (b) Wang, S.; Folting, K.; Streib, W. E.; Schmitt, E. A.; McCusker, J. K.; Hendrickson, D. N.; Christou, G. *Angew. Chem., Int. Ed. Engl.* **1991**, *30*, 305. (c) Libby, E.; McCusker, J. K.; Schmitt, E. A.; Folting, K.; Hendrickson, D. N.; Christou, G. *Inorg. Chem.* **1991**, *30*, 3486. (d) Wemple, M. W.; Tsai, H.-L.; Folting, K.; Hendrickson, D. N.; Christou, G. *Inorg. Chem.* **1993**, *32*, 2025. (e) Wemple, M. W.; Adams, D. M.; Folting, K.; Hendrickson, D. N.; Christou, G. *J. Am. Chem. Soc.* **1995**, *117*, 7275. (f) Wemple, M. W.; Adams, D. M.; Hagen, K. S.; Folting, K.; Hendrickson, D. N.; Christou, G. *J. Chem. Soc., Chem. Commun.* **1995**, 1591.

(13) Wemple, M. W.; Adams, D. M.; Folting, K.; Hagen, K. S.; Hendrickson, D. N.; Christou, G. *Inorg. Chem.*, to be submitted.

(14) Vincent, J. B.; Chang, H.-R.; Folting, K.; Huffman, J. C.; Christou, G.; Hendrickson, D. N. *J. Am. Chem. Soc.* **1987**, *109*, 5703.

(15) Vincent, J. B.; Christmas, C.; Chang, H.-R.; Li, Q.; Boyd, P. D. W.; Huffman, J. C.; Hendrickson, D. N.; Christou, G. *J. Am. Chem. Soc.* **1989**, *111*, 2086.

(16) Wemple, M. W.; Tsai, H.-L.; Wang, S.; Claude, J.-P.; Streib, W. E.; Huffman, J. C.; Hendrickson, D. N.; Christou, G. *Inorg. Chem.* **1996**, *35*, 6450.

collected by filtration, washed with EtOH and then Et_2O, and dried in air. The crude material was recrystallized from CH_2Cl_2/Et_2O. The overall yield was 25−30%. Anal. Calcd (found) for $C_{40}H_{32}N_2O_8ClMn$: C, 63.3 (63.2); H, 4.3 (4.4); N, 3.7 (3.5). Electronic spectrum in MeCN: 310 (38 800), 476 (2280), 510 (1810).

$[Mn_4O_2(O_2CMe)_6(py)_2(dbm)_2]$ (6). To a stirred brown solution of complex **1** (0.87 g, 1.0 mmol) in MeCN (25 mL) was added solid dbmH (0.34 g, 1.5 mmol) in small portions to give a deep brown solution. After several minutes, a red-brown microcrystalline precipitate began to form. Approximately 24 h later, the precipitate was collected by filtration, washed with MeCN, and dried in vacuo; yield 75−80%. Recrystallization from hot MeCN yielded dark red-brown crystals in an overall yield of 60−70%. The crystallographic studies confirmed the title formulation, but dried samples analyzed for $[Mn_4O_2(O_2CMe)_6(py)_2(dbm)_2]\cdot H_2O$, suggesting absorption of H_2O molecules from the atmosphere. Anal. Calcd (found) for $C_{52}H_{52}N_2O_{19}Mn_4$: C, 50.8 (50.5); H, 4.3 (4.1); N, 2.3 (2.1); Mn, 17.9 (17.7). Electronic spectrum in CH_2Cl_2: 336 (35 660), 368 (29 630), 394 (18 360), 454 (2640), 488 (2100), 528 (1010). Selected IR data (cm^{-1}): 1610 (s), 1597 (s), 1587 (s), 1568 (s), 1533 (s), 1522 (s), 1487 (s), 1475 (s), 1441 (s), 1400 (s), 1350 (s), 1334 (s), 1321 (s), 1307 (m, sh), 1226 (m), 1070 (m), 1026 (m), 758 (m), 721(s), 702 (m), 686 (m), 669 (s), 655 (s), 630 (s), 613 (s), 572 (m). When $[Mn_3O(O_2CMe)_6(py)_3](py)$ was employed in place of complex **1**, the same product **6** was obtained in comparable yield, atmospheric O_2 presumably compensating for the lower oxidation state starting material.

$[Mn_4O_2(O_2CEt)_6(py)_2(dbm)_2]$ (7). To a stirred brown solution of $[Mn_3O(O_2CEt)_6(py)_3](ClO_4)$ (0.48 g, 0.50 mmol) in MeCN (20 mL) was added solid dbmH (0.19 g, 0.75 mmol) in small portions to give a deep brown solution. A red-brown microcrystalline solid began to precipitate within minutes. The next day, the solid was collected by filtration, washed with MeCN, and dried; yield 73−88%. The solid analyzed as **7**·H_2O. Anal. Calcd (found) for $C_{58}H_{62}N_2O_{18}Mn_4$: C, 53.06 (53.2); H, 4.91 (4.8); N, 2.13 (2.1); Mn, 16.74 (16.5).

$[Mn_4O_2(O_2CPh)_6(py)(dbm)_2]$ (8). Method A. A solution of complex **2** (1.10 g, 1.0 mmol) in MeCN (60 mL) was filtered, and to the stirred filtrate was added solid dbmH (0.34 g, 1.5 mmol) in small portions to give a homogeneous greenish-brown solution. This was allowed to stand undisturbed for 3 days. The resulting well-formed, essentially black crystals were collected by filtration, washed with MeCN, and dried in vacuo. The yield was 60−65%. No recrystallization was needed. Anal. Calcd (found) for $C_{77}H_{57}NO_{18}Mn_4$: C, 61.49 (61.65); H, 3.82 (3.85); N, 0.93 (0.90); Mn, 14.6 (14.4). Electronic spectrum in CH_2Cl_2: 338 (39 950), 368 (30 770), 390 (17 530), 458 (2180), 484 (1770), 506 (1165). Selected IR data (cm^{-1}): 1608 (s), 1589 (s), 1568 (s), 1522 (s), 1346 (s), 1321 (s), 1305 (s), 1223 (m), 1176 (s), 1070 (m), 1026 (m), 719 (s), 686 (s), 657 (s), 642 (s), 626 (m), 617 (m), 572 (m). When $[Mn_3O(O_2CPh)_6(py)_3](ClO_4)$ was used in place of **2**, the same product was obtained in a comparable yield.

Method B. Solid benzoic acid (1.22 g, 10.0 mmol) was added to a stirred solution of complex **6** (0.60 g, 0.50 mmol) in CH_2Cl_2 (30 mL). The solution was stirred for a further 10 min to dissolve the acid, and the solution was then layered carefully with Et_2O (45 mL). After several days, the resulting black/brown crystals were collected by filtration, washed with Et_2O, and dried in air. The yield was 65−75%. IR spectral examination confirmed that the product was identical with that from method A.

$[Mn_4O_2(O_2CPh)_6(THF)_2(dbm)_2]$ (9). Method A. To a brown solution of complex **2** (0.55 g, 0.50 mmol) in THF (25 mL) was added solid dbmH (0.19 g, 0.75 mmol) in small portions to give a homogeneous brown solution. The solution was filtered and the filtrate layered with Et_2O (40 mL) to give well-formed crystals of **9**·2THF after several days. These were collected by filtration, washed with Et_2O, and dried in air. The yield was 35%. Anal. Calcd (found) for $C_{88}H_{84}O_{22}Mn_4$: C, 61.7 (61.1); H, 4.9 (5.1); Mn, 12.8 (12.5). Electronic spectrum in CH_2Cl_2: 378 (31 730), 460 (3080), 488 (2620). Selected IR data (Nujol): 1610 (s), 1599 (s), 1589 (s), 1572 (s), 1523 (s), 1479 (s), 1348 (s), 1305 (s), 1223 (m), 1176 (m), 1157 (m), 1068 (m), 1045 (m), 1026 (m), 758 (m), 719 (s), 684 (s), 655 (s), 638 (s), 621 (s), 571 (m), 468 (m).

Method B. A red-brown solution of complex **8** in THF was layered with 1.5 volumes of Et_2O to give red-brown crystals after several days in 40−45% yield. The dried sample analyzed as **9**·THF. Anal. Calcd (found) for $C_{84}H_{76}O_{21}Mn_4$: C, 61.5 (62.1); H, 4.7 (4.6); Mn, 13.4 (13.5).

Method C. A slurry of complex **6** (0.30 g, 0.20 mmol) and $PhCO_2H$ (0.61 g, 5.0 mmol) in THF (25 mL) was stirred until all complex **6** had slowly dissolved to give a red-brown solution. The latter was then filtered and the filtrate layered with equivolume Et_2O/hexanes (1:1 v/v). The resulting red-brown crystals were collected by filtration, washed with hexanes, and dried in air. The yield was ∼80%. IR spectral examination confirmed the identity of the product as complex **9**.

$(NBu^n_4)[Mn_4O_2(O_2CPh)_7(dbm)_2]$ (10). Method A. To a stirred red-brown solution of $(Bu^n_4N)[Mn_4O_2(O_2CPh)_9(H_2O)]$ (0.40 g, 0.25 mmol) in CH_2Cl_2 (15 mL) was added solid Na(dbm) (0.125 g, 0.50 mmol). The solution color changed slowly from red-brown to brown over the course of 4 h. A precipitate (NaO_2CPh) was removed by filtration, and the filtrate was treated with Et_2O (15 mL) and hexanes (15 mL). After 2 days, a black crystalline product was isolated by filtration, washed with Et_2O, and dried in air; the yield was 60−70% of **10**·$^1/_4CH_2Cl_2$. Anal. Calcd (found) for $C_{95.25}H_{93.5}NO_{20}Cl_{0.5}Mn_4$: C, 63.22 (63.26); H, 5.21 (5.23); N, 0.77 (0.75); Mn, 12.14 (12.23). Electronic spectrum in CH_2Cl_2: 452 (2390), 514 (1240). Selected IR data (Nujol): 1622 (s, sh), 1612 (s), 1589 (s), 1572 (s), 1533 (s), 1520 (s), 1321 (s), 1304 (s), 1224 (m), 1174 (m), 1157 (w, sh), 1068 (m), 1026 (m), 688 (m), 679 (s), 659 (s), 640 (s), 613 (m), 569 (w), 532 (w), 466 (w).

Method B. A slurry of $(NBu^n_4)[Mn_4O_2(O_2CPh)_8(dbm)]$ (0.35 g, 0.20 mmol) and Na(dbm) (0.050 g, 0.20 mmol) in CH_2Cl_2 (15 mL) was stirred for 4 h. A precipitate (NaO_2CPh) was removed by filtration, and the brown filtrate was treated with Et_2O (15 mL) and hexanes (15 mL) to give a brown precipitate, which was collected by filtration, washed with Et_2O, and dried in air; the yield was 50%. The IR spectrum was identical to that of material prepared by method A.

Conversion of 10 to $(NBu^n_4)[Mn_4O_2(O_2CPh)_7(pic)_2]$. Complex **10**·$^1/_4CH_2Cl_2$ (0.18 g, 0.10 mmol) and picolinic acid (0.028 g, 0.22 mmol) were dissolved in CH_2Cl_2 (10 mL) to give a red-brown solution. After 30 min, Et_2O (10 mL) and hexanes (20 mL) were added, causing the precipitation of a red-brown microcrystalline product, which was collected by filtration, washed with Et_2O, and dried in air. The yield of $(NBu^n_4)[Mn_4O_2(O_2CPh)_7(pic)_2]$, identified by IR spectral comparison with authentic material, was 85%. The same reaction but with Na(pic)·$^3/_4H_2O$ in place of picH gave the same product in ∼65% isolated yield.

$[Mn_4O_3(O_2CPh)_4(dbm)_3]$ (11). Method A. $(NBu^n_4)[Mn_4O_2(O_2CPh)_7(dbm)_2]$ (0.18 g, 0.10 mmol) and $NBu^n_4ClO_4$ (1.00 g, 2.92 mmol) were dissolved in MeCN (10 mL) to give a red-brown solution. The solution was electrolyzed at a potential of 0.65 V versus the ferrocene/ferrocenium (Fc/Fc^+) couple (1.10 V vs SCE); a brown precipitate was slowly produced during the course of the electrolysis. After the electrolysis was complete (60−75 min), the solid was collected by filtration, washed with MeCN, and dried under vacuum; the yield was 30−45% (28−43 mg) based on dbm^- available. Recrystallization from CH_2Cl_2/hexanes gave dark red crystals susceptible to solvent loss. The crystallographic studies confirmed the formulation of the product as **11**·$^3/_2CH_2Cl_2$; however, the dried solid analyzed as solvent-free. Anal. Calcd (found) for $C_{73}H_{53}O_{17}Mn_4$: C, 61.7 (61.4); H, 3.8 (3.8); Mn, 15.5 (15.3). Selected IR data (Nujol): 1599 (s), 1589 (s), 1558 (s), 1523 (vs), 1346 (s), 1323 (s), 1228 (m), 1174 (s), 1070 (m), 1026 (m), 943 (w), 844 (w), 760 (w), 719 (s), 686 (m), 648 (m), 621 (m), 603 (m), 578 (s), 540 (m), 509 (m), 470 (w).

Method B. The yield can be improved by adding dbmH to the electrolysis solution. Thus, dbmH (26.2 mg, 0.117 mmol) in MeCN (5 mL, 0.2 M $NBu^n_4ClO_4$) was added dropwise over 60 min to a solution of complex **10** (0.213 g, 0.117 mmol) in MeCN (20 mL, 0.2 M $TBAClO_4$) that was being electrolyzed at 0.65 V. The rate of addition of the dbmH solution was controlled to roughly parallel the rate of the oxidation of complex **10**. After the electrolysis was complete, the precipitate was collected by filtration, washed with MeCN, and dried under vacuum; the yield was 70−80%. The IR spectrum is identical to that of material prepared by method A.

$[Mn_4O_3(O_2CMe)_4(dbm)_3]$ (12). A slurry of complex **6** (0.24 g, 0.20 mmol) in a solution of 0.2 M $NBu^n_4ClO_4$ or $NBu^n_4PF_6$ in dried MeCN/

Table 1. Crystallographic Data for Complexes **6**, **8**, **11**, and **12**

	6	**8**	**11**	**12**
formula	$C_{52}H_{50}N_2O_{18}Mn_4$	$C_{77}H_{57}NO_{18}Mn_4$	$C_{74.5}H_{56}O_{17}Cl_3Mn_4$[a]	$C_{53}H_{45}O_{17}Mn_4$
fw, g/mol	1210.72	1504.05	1549.38[a]	1173.68
space group	$P\bar{1}$	$P2_1/c$	$P2_1/n$	$P2_1/n$
a, Å	10.868(3)	14.743(6)	15.161(3)	13.549(2)
b, Å	13.864(3)	15.536(8)	21.577(4)	22.338(4)
c, Å	10.625(3)	30.006(13)	22.683(5)	16.618(2)
α, deg	108.62(1)	90	90	90
β, deg	118.98(1)	102.79(1)	108.04(3)	103.74(1)
γ, deg	89.34(2)	90	90	90
V, Å^3	1307	6702	7056	4885
Z	1	4	4	4
T, °C	−131	−155	−100	−171
radiation, Å[b]	0.71069	0.71069	0.71069	0.71069
ρ_{calc}, g/cm^3	1.538	1.491	1.458	1.596
μ, cm^{-1}	9.790	7.789	7.315	10.429
R (R_w or wR2)	3.24 (3.70)[c,d]	4.32 (4.44)[c,d]	8.63 (21.80)[c,e]	4.63 (4.45)[c,d]

[a] Including $^3/_2CH_2Cl_2$ solvate molecules. [b] Graphite monochromator. [c] $R = 100\sum||F_o| - |F_c||/\sum|F_o|$. [d] $R_w = 100[\sum w(|F_o| - |F_c|)^2/\sum w|F_o|^2]^{1/2}$ where $w = 1/\sigma^2(|F_o|)$. [e] wR2 $= 100[\sum w(F_o^2 - F_c^2)^2/\sum wF_o^4]^{1/2}$.

CH_2Cl_2 (3:1) (16 mL) was electrolyzed at 0.84 V (vs Fc/Fc^+) under an argon atmosphere. During the electrolysis, a solution of dbmH (0.045 g, 0.20 mmol) in 0.2 M $(NBu^n_4)(ClO_4)$ or $(NBu^n_4)(PF_6)$ in dried MeCN (5 mL) was slowly added dropwise. When the electrolysis was complete (60−90 min), the precipitated solid was collected by filtration under anaerobic conditions, washed with MeCN, and dried in vacuo. The yield was typically 45−55%. Anal. Calcd (found) for $C_{53}H_{45}O_{17}Mn_4$: C, 54.24 (53.84); H, 3.86 (3.88). Selected IR data (Nujol): 1680 (m), 1597 (m), 1588 (m), 1568 (m), 1534 (s), 1522 (s), 1353 (s), 1339 (s), 1325 (s), 1254 (m), 1233 (m), 1076 (m), 1047 (w), 1024 (m), 945 (m), 785 (w), 772 (m), 731 (m), 704 (w), 693 (m), 648 (m), 612 (m), 590 (m), 573 (m), 544 (m), 523 (m), 473 (w). A CH_2Cl_2 solution of this solid was layered with MeCN and stored at 5 °C to give X-ray quality crystals. $[Mn_4O_3(O_2CCD_3)_4(dbm)_3]$ can be prepared in an analogous manner using $[Mn_4O_2(O_2CCD_3)_6(py)_2(dbm)_2]$.

X-ray Crystallography and Solution of Structures. Data were collected on complexes **6**, **8**, and **12** at the IUMSC, and on complex **11**·$^3/_2CH_2Cl_2$ at Emory University. Details of the diffractometry, low-temperature facilities, and computational procedures employed by the Molecular Structure Center are available elsewhere.[17] Data collection parameters and structure solution details are listed in Table 1. The structures were solved by standard methods (MULTAN78 or SHELXL-92) and Fourier techniques and refined on *F* or F^2 by a full-matrix least-squares approach.

For complex **6**, a suitable crystal (0.25 × 0.30 × 0.35 mm) was affixed to a glass fiber using silicone grease and transferred to a goniostat, where it was cooled to −131 °C for characterization and data collection ($+h, \pm k, \pm l$; $6° \le 2\theta \le 45°$). A systematic search of a limited hemisphere of reciprocal space revealed no Laue symmetry or systematic absences. An initial choice of space group $P\bar{1}$ was subsequently confirmed by the successful solution of the structure. Following intensity data collection, data processing gave a residual of 0.020 for 657 unique intensities which had been measured more than once. Four standards measured every 300 data showed no significant trends. No correction was made for absorption. After the non-hydrogen atoms had been located and partially refined, a difference Fourier map phased on the non-hydrogen atoms revealed most of the hydrogen atom positions. In the final cycles of least-squares refinement, the non-hydrogen atoms were varied with anisotropic thermal parameters and the hydrogen atoms were varied with isotropic thermal parameters. The final difference map was essentially featureless, the largest peak being 0.66 e/Å^3.

For complex **8**, a suitable crystal (0.25 × 0.25 × 0.25 mm) was located and transferred to the goniostat as above for characterization and data collection ($+h, +k, \pm l$; $6° \le 2\theta \le 45°$) at −155 °C. A systematic search of a limited hemisphere of reciprocal space located a set of diffraction maxima with Laue symmetry and systematic absences corresponding to the unique monoclinic space group $P2_1/c$. Subsequent solution and refinement of the structure confirmed this choice. The *R* for averaging of equivalent reflections measured more than once was 0.053. All non-hydrogen atoms were readily located and refined with anisotropic thermal parameters. A difference Fourier map phased on the non-hydrogen atoms revealed the location of some, but not all, hydrogen atoms. All hydrogen atom positions were therefore calculated using idealized geometries and d(C−H) = 0.95 Å. The hydrogen atoms were included as fixed atom contributors at these calculated positions for the final cycles of refinement. No absorption correction was performed. The final difference Fourier map was essentially featureless, with the largest peak being 0.53 e/Å^3.

For complex **11**·$^3/_2CH_2Cl_2$, a suitable crystal (0.10 × 0.33 × 0.70 mm) was located while the sample was in mineral oil to prevent solvent loss and transferred to the goniostat as above for characterization and data collection ($+h, +k, \pm l$; $1° \le 2\theta \le 45°$) at −100 °C. A systematic search of a limited hemisphere of reciprocal space located a set of diffraction maxima with Laue symmetry and systematic absences corresponding to monoclinic space group $P2_1/n$, which was confirmed by the subsequent successful solution of the structure. The *R* for averaging equivalent reflections measured more than once was 0.0623. All non-hydrogen atoms were readily located and refined with anisotropic thermal parameters; the phenyl rings were included as rigid bodies with C−C bond lengths of 1.39 Å and C−C− angles of 120°. In the final cycles of least-squares refinement on F^2, the hydrogen atoms were included with isotropic thermal parameters. The final difference Fourier map was essentially featureless, the largest peak being 0.90 e/Å^3.

For complex **12**, a suitable crystal (0.10 × 0.24 × 0.30 mm) was located and transferred to the goniostat as above for characterization and data collection ($+h, +k, \pm l$; $6° \le 2\theta \le 45°$) at −171 °C. A systematic search of a limited hemisphere of reciprocal space yielded a set of reflections which exhibited monoclinic diffraction symmetry (2/*m*). The systematic extinction of *h*01 for $h + 1 = 2n + 1$ and of 0*k*0 for $k = 2n + 1$ identified the space group as $P2_1/n$, confirmed by the subsequent solution and refinement of the structure. The *R* was 0.042 for the averaging of 5320 equivalent reflections measured more than once. Plots of the four standard reflections measured every 300 reflections showed no significant trends. No absorption correction was performed. All non-hydrogen atoms were readily located. Many of the hydrogen atoms were evident in a difference Fourier map phased on the non-hydrogen atoms. Hydrogen atoms were introduced in fixed, idealized positions, with a C−H distance of 0.95 Å and individual isotropic thermal parameters equal to 1.0 plus the isotropic equivalent of the parent atom; it should be noted that all of the methyl groups had at least one hydrogen atom located. The final difference map was essentially featureless, the largest peak being 0.42 e/Å^3.

For all complexes, the values of discrepancy indices *R* and R_w, or *R* and wR2, are included in Table 1.

(17) Chisholm, M. H.; Folting, K.; Huffman, J. C.; Kirkpatrick, C. C. *Inorg. Chem.* **1984**, *23*, 1021.

Other Studies. Infrared and electronic spectra were recorded on Nujol mulls between KBr plates or in solution, respectively, using Nicolet 510P FTIR and Hewlett Packard 8452A spectrophotometers. Cyclic voltammograms (CV) and differential pulse voltammograms (DPV) were recorded on a BAS CV50W voltammetric analyzer: measurements were performed at room temperature using a glassy carbon working electrode, a Pt wire auxiliary electrode, and an SCE reference electrode. Potentials are quoted vs the ferrocene/ferrocenium couple under the same conditions. No IR compensation was employed. Controlled potential electrolyses were performed with a similar three-electrode system using a high surface area Pt basket electrode. The supporting electrolytes were $NBu^n_4ClO_4$ or $NBu^n_4PF_6$. ^{1}H NMR spectroscopy was performed using a Varian XL-300 instrument; chemical shifts are quoted using the δ scale (shifts downfield are positive). Variable-temperature magnetic susceptibility data were obtained with a Quantum Design MPMS5 SQUID susceptometer equipped with a 5.5 T magnet. Pascal's constants were used to estimate the diamagnetic correction for each complex, which was subtracted from the experimental susceptibility to give the molar magnetic susceptibility (χ_M).

Results

Syntheses. The transformations involving complexes **1**−**9** summarized below and the complex numbering scheme are presented for convenience in Scheme 1.

The reactions of the trinuclear complexes **1** and **2** with β-diketones represent an excellent entry point into tetranuclear Mn/O complexes with a predominantly or completely O-based ligation environment. AcacH itself is of little use, however, because it is too susceptible to oxidation by good oxidizing agents such as Mn^{III}; the oxidation of acacH by metal ions has been well documented.[18] Thus, treatment of **2** (Mn^{II},2Mn^{III}) with acacH leads to 45−60% isolated yields of the 4Mn^{II},2Mn^{III} complex $[Mn_6O_2(O_2CPh)_{10}L_4]$ (**3**), where 4L = $(MeCN)_2(H_2O)_2$ (**3a**) or $(DMF)_4$ (**3b**) after recrystallization from DMF/Et_2O/hexanes. As discussed previously,[19] this conversion is rationalized as due to initial reduction of the $[Mn_3O]^{6+}$ core followed by dimerization (eq 1). Much more resistant to oxidation are

$$[Mn_3O]^{6+} + e^- \rightarrow [Mn_3O]^{5+} \rightarrow {}^1/_2[Mn_6O_2]^{10+} \qquad (1)$$

dbmH and dbm^-. Thus, reactions of **1** and **2** with dbmH lead to Mn^{III} products. In mapping out such reactions, it was found that dbmH:$[Mn_3O]$ ratios of 3:1 or greater give, as the main product, the mononuclear complex $Mn(dbm)_3$ (**4**), or $[Mn(dbm)_2(py)_2](ClO_4)$ (**5**) if an excess of pyridine is present. With a dbmH:$[Mn_3O]$ ratio of 3:2 employing complex **1**, however, the product is $[Mn_4O_2(O_2CMe)_6(py)_2(dbm)_2]$ (**6**), analogous to the earlier reactions with bpy[10] or picH,[20] which gave $[Mn_4O_2(O_2CMe)_7(bpy)_2]^+$ and $[Mn_4O_2(O_2CMe)_7(pic)_2]^-$ products, respectively. Similarly, the reaction of $[Mn_3O(O_2CEt)_6(py)_3](ClO_4)$ with dbmH gives $[Mn_4O_2(O_2CEt)_6(py)_2(dbm)_2]$ (**7**). The analogous reaction with complex **2** gave essentially the same type of product, although the complex $[Mn_4O_2(O_2CPh)_6(py)(dbm)_2]$ (**8**) contains only one py group, suggesting one Mn^{III} ion to be five-coordinate, a relatively unusual coordination number for Mn^{III} with such ligation; this was subsequently confirmed by a crystallographic study (vide infra). The cause may be steric congestion between the many Ph rings of hypothetical $[Mn_4O_2(O_2CPh)_6(py)_2(dbm)_2]$. Recrystallization of **8** from THF, reaction of **2** with dbmH in THF, or reaction of **6** with an excess of $PhCO_2H$ in THF all gave $[Mn_4O_2(O_2CPh)_6(THF)_2(dbm)_2]$ (**9**), containing two THF groups presumably due to the greater flexibility of THF vs rigid py groups. In contrast, reaction of **6** with $PhCO_2H$ in CH_2Cl_2 gives **8**, again with a single py ligand. The reaction of **8** with an excess of py (25 equiv) caused core degradation, and the isolated product in 79% yield was the known $[Mn_6O_2(O_2CPh)_{10}(py)_4]$.[19]

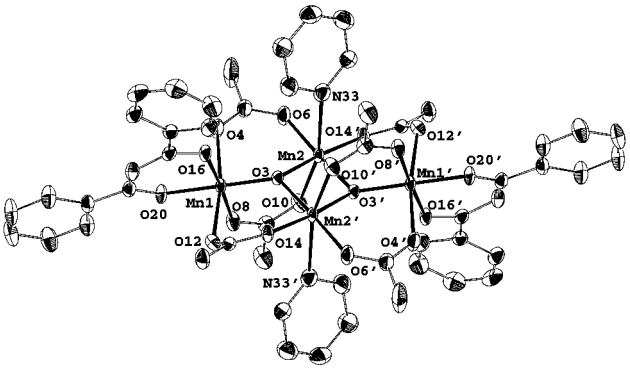

Figure 1. ORTEP representation at the 50% probability level of $[Mn_4O_2(O_2CMe)_6(py)_2(dbm)_2]$ (**6**). Primed and unprimed atoms are related by an inversion center.

The complex $(NBu^n_4)[Mn_4O_2(O_2CPh)_7(dbm)_2]$ (**10**) is not available from the reactions between dbmH and $[Mn_3O]$ species explored to date, but it can be conveniently prepared in high yield (60−70%) from the reaction of Na(dbm) with (NBu^n_4)-$[Mn_4O_2(O_2CPh)_9(H_2O)]$ or $(NBu^n_4)[Mn_4O_2(O_2CPh)_8(dbm)]$, the latter itself being obtained from the former as described elsewhere.[16] This can be summarized in eq 2. Complex **10** will undergo chelate substitution with picolinic acid to give $[Mn_4O_2(O_2CPh)_7(pic)_2]^-$ in high yield (85%) (eq 3). It was of interest to find the exchange to be so clean rather than the picolinate substituting at a benzoate position to give products containing both dbm^- and pic^-. The observed exchange is presumably facilitated by the protonation of dbm^- (pK_a of dbmH = 8.95) by picH (pK_a = 5.39).[21]

$$[Mn_4O_2(O_2CPh)_9(H_2O)]^- + 2Na(dbm) \rightarrow [Mn_4O_2(O_2CPh)_7(dbm)_2]^- + 2NaO_2CPh + H_2O \qquad (2)$$

$$[Mn_4O_2(O_2CPh)_7(dbm)_2]^- + 2picH \rightarrow [Mn_4O_2(O_2CPh)_7(pic)_2]^- + 2dbmH \qquad (3)$$

Structures of Complexes 6 and 8. ORTEP representations of **6** and **8** are shown in Figures 1 and 2, respectively. Selected interatomic distances and angles are listed in Tables 2 and 3, respectively.

Complex **6** crystallizes in triclinic space group $P\bar{1}$ with the molecule lying on an inversion center. The $[Mn_4(\mu_3\text{-}O)_2]^{8+}$ core thus contains an exactly planar Mn_4 parallelogram with Mn1···Mn2 (3.308(1) Å) slightly shorter than Mn1···Mn2′ (3.398(1) Å), consistent with two vs one $MeCO_2^-$ bridges across these Mn_2 pairs. The μ_3-O^{2-} ions O3′ and O3′ are 0.325 Å above and below their Mn_3 planes and give a central $[Mn_2O_2]$ rhomb with a short Mn2···Mn2′ distance (2.875(1) Å). In addition to a total of six bridging $MeCO_2^-$ groups, there are two chelating dbm^- groups at the two ends and two terminal py groups on the central Mn atoms, completing six-coordinate, near-octahedral

(18) Bhattacharjee, M. N.; Chadhuri, M. K.; Khathing, D. T. *J. Chem. Soc., Dalton Trans.* **1982**, 669.
(19) Schake, A. R.; Vincent, J. B.; Li, Q.; Boyd, P. D. W.; Folting, K.; Huffman, J. C.; Hendrickson, D. N.; Christou, G. *Inorg. Chem.* **1989**, *28*, 1915.
(20) Libby, E.; McCusker, J. K.; Schmitt, E. A.; Folting, K.; Hendrickson, D. N.; Christou, G. *Inorg. Chem.* **1991**, *30*, 3486.
(21) Serjeant, E. P.; Dempsey, B. *Ionization Constants of Organic Acids in Aqueous Solution*; Pergamon: New York, 1979.

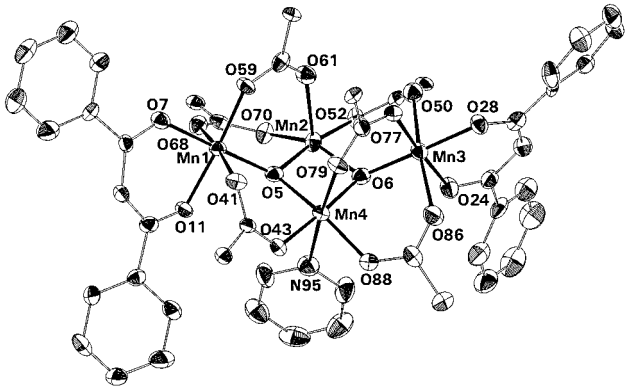

Figure 2. ORTEP representation at the 50% probability level of $[Mn_4O_2(O_2CPh)_6(py)(dbm)_2]$ (**8**). For clarity, only the *ipso*-carbon of each benzoate phenyl ring is shown.

Table 2. Selected Interatomic Distances (Å) and Angles (deg) for $[Mn_4O_2(O_2CMe)_6(py)_2(dbm)_2]$ (**6**)

Mn(1)···Mn(2)	3.308(1)	Mn(1)−O(20)	1.925(2)
Mn(1)···Mn(2)′	3.398(1)	Mn(2)−O(3)	1.885(2)
Mn(2)···Mn(2)′	2.875(1)	Mn(2)−O(3)′	1.894(2)
Mn(1)−O(3)	1.877(2)	Mn(2)−O(6)	1.957(2)
Mn(1)−O(4)	2.136(2)	Mn(2)−O(10)	2.187(2)
Mn(1)−O(8)	1.928(2)	Mn(2)−O(14)	1.953(2)
Mn(1)−O(12)	2.206(2)	Mn(2)−N(33)	2.410(2)
Mn(1)−O(16)	1.931(2)		
O(3)−Mn(1)−O(4)	94.72(8)	O(3)−Mn(2)−O(6)	100.14(9)
O(3)−Mn(1)−O(8)	95.01(9)	O(3)′−Mn(2)−O(10)	96.97(9)
O(3)−Mn(1)−O(12)	92.88(8)	O(3)−Mn(2)−O(10)	88.27(8)
O(3)−Mn(1)−O(16)	87.74(8)	O(3)−Mn(2)−O(14)′	175.15(9)
O(3)−Mn(1)−O(20)	176.89(8)	O(3)′−Mn(2)−O(14)′	95.05(9)
O(4)−Mn(1)−O(8)	93.37(9)	O(3)′−Mn(2)−N(33)	98.52(9)
O(4)−Mn(1)−O(12)	169.81(8)	O(3)−Mn(2)−N(33)	88.59(9)
O(4)−Mn(1)−O(16)	88.96(9)	O(6)−Mn(2)−O(10)	85.53(9)
O(4)−Mn(1)−O(20)	86.79(9)	O(6)−Mn(2)−O(14)′	84.00(9)
O(8)−Mn(1)−O(12)	92.71(9)	O(6)−Mn(2)−N(33)	79.09(10)
O(8)−Mn(1)−O(16)	176.23(8)	O(10)−Mn(2)−O(14)′	89.54(8)
O(8)−Mn(1)−O(20)	87.60(9)	O(10)−Mn(2)−N(33)	163.50(9)
O(12)−Mn(1)−O(16)	84.57(8)	O(14)′−Mn(2)−N(33)	94.72(9)
O(12)−Mn(1)−O(20)	85.30(8)	Mn(1)−O(3)−Mn(2)	123.17(10)
O(16)−Mn(1)−O(20)	89.58(9)	Mn(1)−O(3)−Mn(2)′	128.61(10)
O(3)−Mn(2)−O(3)′	80.93(9)	Mn(2)−O(3)−Mn(2)′	99.07(9)
O(3)′−Mn(2)−O(6)	177.33(9)		

geometry at each metal. The symmetry is C_i. All metals show clear evidence of Jahn−Teller (JT) distortions, as expected for high-spin Mn^{III} (d^4) in near-octahedral geometry, taking the form of axial elongation along the O4−Mn1−O12 and O10−Mn2−N33 axes; the former and latter are approximately parallel and perpendicular, respectively, to the Mn_4 plane. As is expected, the JT axes are oriented as to avoid the $Mn-O^{2-}$ bonds, which are the shortest and strongest in the molecule (<1.9 Å).

Complex **8** crystallizes in monoclinic space group $P2_1/c$ with a complete molecule in the asymmetric unit. As for **6**, there is a $[Mn_4(\mu_3\text{-}O)_2]^{8+}$ core, but the Mn_4 unit now has a bent or "butterfly" arrangement, with Mn1 and Mn3 the "wingtip" atoms and Mn2 and Mn4 the "body" atoms of the butterfly. O5 and O6 lie 0.299 and 0.399 Å below their Mn_3 planes. Peripheral ligation is again by bridging carboxylate, terminal py, and chelating dbm^- groups, but now there is only one py on the central metals, with Mn2 consequently being five-coordinate, an unusual coordination number for Mn^{III} with such ligands. The geometry at Mn2 is essentially square-pyramidal (sp) with O61 occupying the apex and consequently yielding a Mn2−O61 bond (2.076(5) Å) noticeably longer than the basal Mn−O (carboxylate) bonds (1.941(5) Å). Consideration of the angles about Mn2 gives a τ value of 0.27 ($\tau = 0$ and 1 for sp and tbp geometries, respectively[22]), indicating significant but not severe distortion from sp geometry. The five-coordination at Mn2 causes a slight shortening of $Mn2-O^{2-}$ distances (average 1.870 Å) compared with Mn4 (average 1.891 Å). Again, the six-coordinate Mn^{III} atoms show JT elongations, along the O41−Mn1−O68, O50−Mn3−O86, and O79−Mn4−O95 axes.

Table 3. Selected Interatomic Distances (Å) and Angles (deg) for $[Mn_4O_2(O_2CPh)_6(py)(dbm)_2]$ (**8**)

Mn(3)···Mn(4)	3.299(2)	Mn(2)−O(61)	2.076(5)
Mn(1)···Mn(4)	3.425(2)	Mn(2)−O(70)	1.941(5)
Mn(1)···Mn(2)	3.327(2)	Mn(3)−O(6)	1.872(5)
Mn(2)···Mn(3)	3.360(2)	Mn(3)−O(24)	1.941(5)
Mn(2)···Mn(4)	2.820(2)	Mn(3)−O(28)	1.911(5)
Mn(1)−O(5)	1.892(4)	Mn(3)−O(50)	2.200(5)
Mn(1)−O(7)	1.923(5)	Mn(3)−O(77)	1.932(5)
Mn(1)−O(11)	1.942(4)	Mn(3)−O(86)	2.172(5)
Mn(1)−O(41)	2.193(5)	Mn(4)−O(5)	1.892(5)
Mn(1)−O(59)	1.939(4)	Mn(4)−O(6)	1.891(5)
Mn(1)−O(68)	2.165(5)	Mn(4)−O(43)	1.926(5)
Mn(2)−O(5)	1.859(5)	Mn(4)−O(79)	2.145(4)
Mn(2)−O(6)	1.882(5)	Mn(4)−O(88)	1.957(5)
Mn(2)−O(52)	1.941(5)	Mn(4)−N(95)	2.404(6)
O(5)−Mn(1)−O(7)	178.45(19)	O(24)−Mn(3)−O(50)	85.03(19)
O(5)−Mn(1)−O(11)	92.20(18)	O(24)−Mn(3)−O(77)	176.42(20)
O(5)−Mn(1)−O(41)	88.51(19)	O(24)−Mn(3)−O(86)	85.55(20)
O(5)−Mn(1)−O(59)	93.90(19)	O(28)−Mn(3)−O(50)	87.50(19)
O(5)−Mn(1)−O(68)	88.57(19)	O(28)−Mn(3)−O(77)	86.58(19)
O(7)−Mn(1)−O(11)	89.10(18)	O(28)−Mn(3)−O(86)	90.45(19)
O(7)−Mn(1)−O(41)	92.47(19)	O(50)−Mn(3)−O(77)	94.38(18)
O(7)−Mn(1)−O(59)	84.85(19)	O(50)−Mn(3)−O(86)	170.36(18)
O(7)−Mn(1)−O(68)	90.60(19)	O(77)−Mn(3)−O(86)	94.90(19)
O(11)−Mn(1)−O(41)	83.07(18)	O(5)−Mn(4)−O(6)	82.17(20)
O(11)−Mn(1)−O(59)	172.91(19)	O(5)−Mn(4)−O(43)	95.47(20)
O(11)−Mn(1)−O(68)	90.09(19)	O(5)−Mn(4)−O(79)	98.64(18)
O(41)−Mn(1)−O(59)	93.46(19)	O(5)−Mn(4)−O(88)	166.69(20)
O(41)−Mn(1)−O(68)	172.46(18)	O(5)−Mn(4)−N(95)	83.44(20)
O(59)−Mn(1)−O(68)	93.67(19)	O(6)−Mn(4)−O(43)	176.65(20)
O(5)−Mn(2)−O(6)	83.30(20)	O(6)−Mn(4)−O(79)	89.94(18)
O(5)−Mn(2)−O(52)	171.29(20)	O(6)−Mn(4)−O(88)	94.87(20)
O(5)−Mn(2)−O(61)	93.69(18)	O(6)−Mn(4)−N(95)	86.35(20)
O(5)−Mn(2)−O(70)	94.70(20)	O(43)−Mn(4)−O(79)	88.06(18)
O(6)−Mn(2)−O(52)	93.05(20)	O(43)−Mn(4)−O(88)	87.96(20)
O(6)−Mn(2)−O(61)	107.14(19)	O(43)−Mn(4)−N(95)	95.77(20)
O(6)−Mn(2)−O(70)	155.32(19)	O(79)−Mn(4)−O(88)	94.32(19)
O(52)−Mn(2)−O(61)	94.94(19)	O(79)−Mn(4)−N(95)	175.47(19)
O(52)−Mn(2)−O(70)	85.31(19)	O(88)−Mn(4)−N(95)	83.42(20)
O(61)−Mn(2)−O(70)	97.53(19)	Mn(1)−O(5)−Mn(2)	124.98(24)
O(6)−Mn(3)−O(24)	88.19(19)	Mn(1)−O(5)−Mn(4)	129.70(24)
O(6)−Mn(3)−O(28)	176.29(21)	Mn(2)−O(5)−Mn(4)	97.48(21)
O(6)−Mn(3)−O(50)	89.18(19)	Mn(2)−O(6)−Mn(3)	127.06(24)
O(6)−Mn(3)−O(77)	95.34(19)	Mn(2)−O(6)−Mn(4)	96.71(21)
O(6)−Mn(3)−O(86)	92.55(19)	Mn(3)−O(6)−Mn(4)	122.49(25)
O(24)−Mn(3)−O(28)	89.86(19)		

Magnetochemistry of $[Mn_4O_2(O_2CMe)_6(py)_2(dbm)_2]$ (6). Variable-temperature, solid-state magnetic susceptibility data were collected on powdered samples of **6** in the 10.0−279 K range. The effective magnetic moment (μ_{eff} per Mn_4) decreases gradually from 7.51 μ_B at 279 K to 6.08 μ_B at 50.1 K, and then decreases more rapidly to 4.12 μ_B at 10.0 K. This is similar to the behavior already described in detail previously for $(NBu^n_4)[Mn_4O_2(O_2CMe)_7(pic)_2]$.[20] The data were fit to the same theoretical χ_m vs T expression employed for the pic^- complex, where J_{wb} and J_{bb} are the wingtip/body and body/body exchange interactions, respectively, and which includes the effects of zero-field splitting in the ground state (responsible for the rapid decrease in μ_{eff} at the lowest temperatures). The fitting parameters were $J_{wb} = -5.6$ cm^{-1}, $J_{bb} = -21.9$ cm^{-1}, $g = 1.88$, and $D = 3.82$ cm^{-1}; temperature independent paramagnetism was held constant at 800×10^{-6} cm^3 mol^{-1}. These data indicate a $S = 3$ ground state for complex **6**, in agreement with the same value previously determined for $(NBu^n_4)[Mn_4O_2(O_2CMe)_7(pic)_2]$[20] and $[Mn_4O_2(O_2CMe)_7(bpy)_2](ClO_4)$,[15] and shown

(22) Addison, A. W.; Rao, T. N.; Reedijk, J.; Rijn, J.; Verschoor, G. C. *J. Chem. Soc., Dalton Trans.* **1984**, 1349.

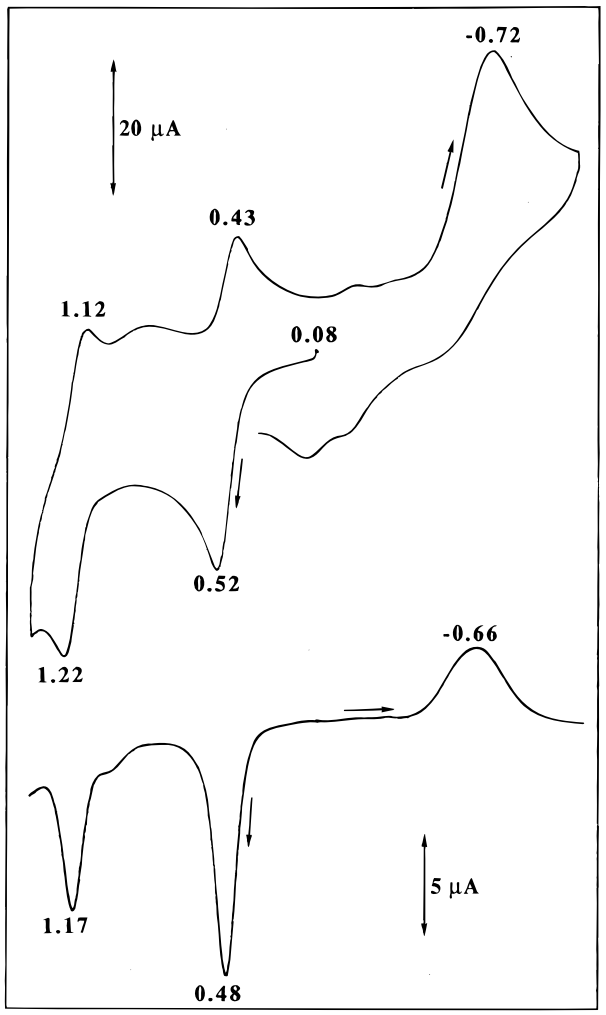

Figure 3. CV (top) and DPV (bottom) scans of $(NBu^n_4)[Mn_4O_2(O_2CPh)_7(dbm)_2]$ (**10**) in MeCN; the scan rates were 100 and 5 mV/s, respectively. The potentials are given vs ferrocene under identical conditions.

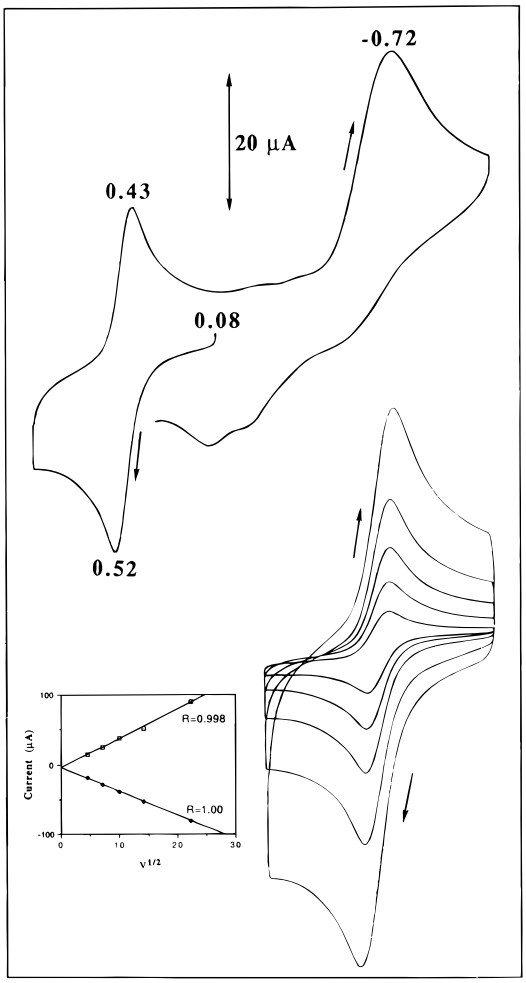

Figure 4. CV scan of complex **10** in MeCN showing only the first, reversible oxidation, and a scan rate (ν) dependence in the 20−500 mV/s range; the inset is a plot of the peak current vs $\nu^{1/2}$ for the forward and reverse scans.

to be a consequence of the competing J_{wb} and J_{bb} exchange parameters.

Electrochemical Studies. Complexes **6** and **8**−**10** were investigated by cyclic voltammetry (CV) and differential pulse voltammetry (DPV). Complex **10** displayed the most reversible behavior; its CV and DPV traces in MeCN are shown in Figure 3 and consist of an irreversible reduction at ~ -0.7 V and two oxidation processes at 0.48 and 1.17 V vs ferrocene, the first of which appears quasi-reversible in the DPV trace but not so in the CV scan. However, if the CV switching potential is set at a value less positive than for the second oxidation, the resulting CV scan (Figure 4) looks much more like that expected for a reversible process, with i_f/i_r approaching unity (i_f and i_r are the forward and reverse currents), and plots of peak current vs the square root of scan rate being linear in the 20−500 mV/s range, suggesting a diffusion-controlled process. The observed CV/DPV behavior suggests the electron-transfer series of eq 4,

$$[Mn_4O_2]^{10+} \xleftarrow{1.17\ V} [Mn_4O_2]^{9+} \rightleftharpoons^{0.48\ V} [Mn_4O_2]^{8+} \xrightarrow{-0.66\ V} [Mn_4O_2]^{7+} \quad (4)$$

with only the first oxidation appearing reversible on the electrochemical time scale. In contrast, the neutral complexes **6**, **8**, and **9** do not display behavior that approaches reversibility on the electrochemical time scale. Figure 5 shows the results for **6**: an oxidation at 0.61 V is well observed (albeit broad) in the DPV but not the CV scan where the reverse wave is not particularly well formed. The reductions are again irreversible. In addition, there are several small features reproducibly seen in analytically pure material suggesting more than one species in solution, probably those formed by py dissociation and/or py/MeCN exchange. Additional, very irreversible oxidation processes are evident at more positive potentials than those shown in Figure 5. The main conclusion from the electrochemical studies is thus that the $[Mn_4O_2]^{8+}$ complexes display oxidation processes in MeCN but that only for **10** is reversibility by electrochemical criteria approached.

Controlled Potential Electrolysis (CPE) Studies. In order to probe the stability and/or reactivity of oxidized **10** on a longer time scale, CPE studies were performed in distilled MeCN under argon at a potential of 0.65 V. A solid was found to precipitate during the course of the electrolysis (60−75 min), and this was subsequently identified to be not the one-electron-oxidized version of **10**, but instead $[Mn_4O_3(O_2CPh)_4(dbm)_3]$ (**11**) (eq 5) in a yield of 10%. Consideration of the formulas of **10** and **11**

$$[Mn_4O_2(O_2CPh)_7(dbm)_2]^- \xrightarrow[MeCN]{0.65\ V} [Mn_4O_3(O_2CPh)_4(dbm)_3] \quad (5)$$

indicates that a one-electron oxidation from a $4Mn^{III}$ to a $3Mn^{III}$,

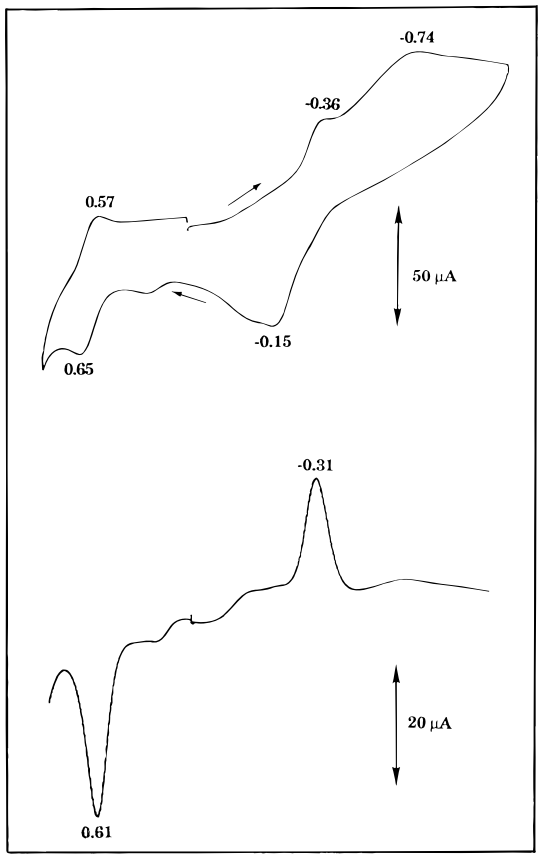

Figure 5. CV (top) and DPV (bottom) scans of $[Mn_4O_2(O_2CMe)_6(py)_2(dbm)_2]$ (**6**) in MeCN at 100 and 5 mV/s, respectively. The potentials are vs ferrocene.

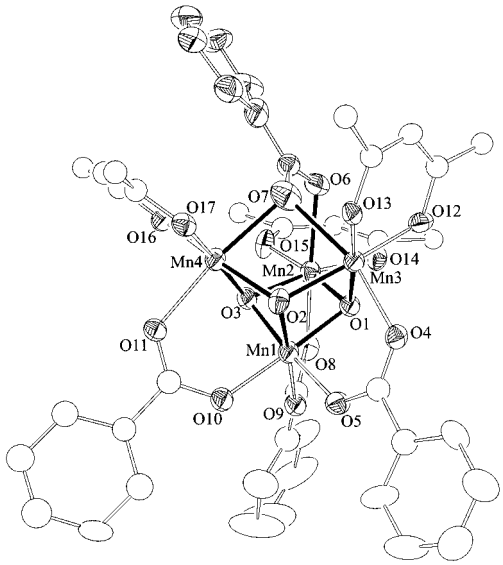

Figure 6. ORTEP representation at the 50% probability level of $[Mn_4O_3(O_2CPh)_4(dbm)_3]$ (**11**). For clarity, only the *ipso*-carbon atom of each dbm phenyl ring is shown.

Mn^{IV} product had indeed occurred, but that the product had increased O^{2-}:Mn *and* dbm:Mn ratios compared with **10**. Thus, the CPE was repeated under a variety of conditions and the following observations were made: (i) use of undistilled MeCN under air gave an increased yield of **11** of 20−30%; (ii) addition of dbmH to the filtrate from (i) resulted in precipitation of more **11** for a total yield of 40−45%, and (iii) addition of 1 equiv of dbmH to the solution *before* electrolysis gave a reduced yield of ∼25%. These observations suggested that, upon oxidation

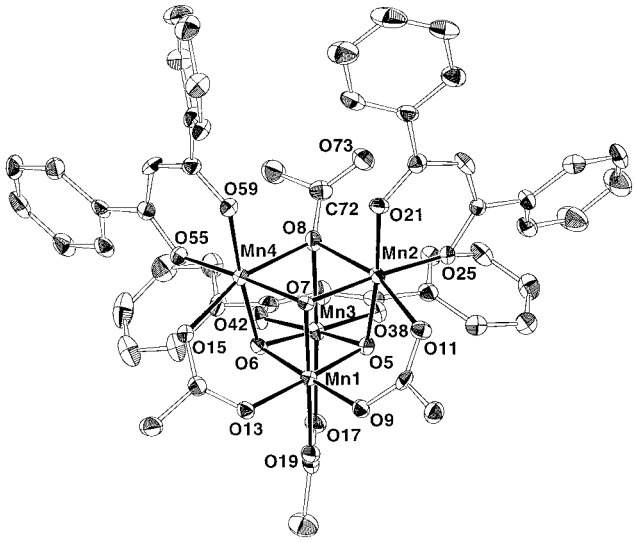

Figure 7. ORTEP representation at the 50% probability level of $[Mn_4O_3(O_2CMe)_4(dbm)_3]$ (**12**).

of **10**, the generated species reacts with H_2O and undergoes a rearrangement involving additional dbm incorporation to give **11**. This allowed the procedure described in the Experimental Section (method B) to be developed: the CPE was carried out in air in undistilled MeCN with 1 equiv of dbmH added dropwise over ∼ 60 min; the yield under these conditions is reproducibly in the 70−80% range. The transformation may now be summarized as in eq 6.

$$[Mn_4O_2(O_2CPh)_7(dbm)_2]^- + H_2O + dbmH \xrightarrow{-e^-} [Mn_4O_3(O_2CPh)_4(dbm)_3] + 3PhCO_2H \quad (6)$$

Given these results for **10**, CPE was also performed on complex **6**. After preliminary experimentation, which showed that a mixed-solvent system ($MeCN:CH_2Cl_2 = 3:1$) was required to cause product precipitation and that this product was sensitive to subsequent reaction with air, the procedure under argon in the Experimental Section was developed that leads to isolation of $[Mn_4O_3(O_2CMe)_4(dbm)_3]$ (**12**) in 45−55% yield. This is summarized in eq 7. Thus, the CPE of **6** proceeds analogously to that of **10** with a similar (but *not* structurally identical) product (vide infra).

$$[Mn_4O_2(O_2CMe)_6(py)_2(dbm)_2] + dbmH + H_2O \xrightarrow{-e^-} [Mn_4O_3(O_2CMe)_4(dbm)_3] + 2MeCO_2H + pyH^+ + py \quad (7)$$

Structures of Complexes 11 and 12. ORTEP representations of **11** and **12** are shown in Figures 6 and 7, respectively, and selected interatomic distances and angles are listed in Tables 4 and 5.

Complex **11** crystallizes in monoclinic space group $P2_1/n$ with the Mn_4 molecule in a general position. The structure consists of a Mn_4 trigonal pyramid with the Mn^{IV} ion Mn(1) at the apex. The three vertical faces are capped by a μ_3-$PhCO_2^-$ group ligated through both its O atoms, with O(6) terminal to Mn(2) and O(7) bridging Mn(3) and Mn(4). The latter O atom O(7) does not bridge symmetrically, however; Mn(3)−O(7) (2.267(10) Å) is noticeably longer than Mn(4)−O(7) (2.173(9) Å). This asymmetry is also seen in the resulting $Mn^{III}\cdots Mn^{III}$ separations: as expected, Mn(3)···Mn(4) (3.197(2) Å) is the shortest, but the others are noticeably different, with Mn(2)···Mn(3) (3.277(2) Å) much shorter than Mn(2)···Mn(4) (3.432(2) Å).

Table 4. Selected Interatomic Distances (Å) and Angles (deg) for $[Mn_4O_3(O_2CPh)_4(dbm)_3]$ (**11**)

Mn(1)···Mn(2)	2.802(3)	Mn(2)···Mn(3)	3.277(2)
Mn(1)···Mn(3)	2.780(2)	Mn(2)···Mn(4)	3.432(2)
Mn(1)···Mn(4)	2.787(3)	Mn(3)···Mn(4)	3.197(2)
Mn(1)−O(2)	1.835(7)	Mn(3)−O(13)	1.900(7)
Mn(1)−O(1)	1.856(8)	Mn(3)−O(1)	1.912(7)
Mn(1)−O(3)	1.859(8)	Mn(3)−O(2)	1.942(7)
Mn(1)−O(5)	1.912(8)	Mn(3)−O(4)	2.169(7)
Mn(1)−O(10)	1.941(8)	Mn(3)−O(7)	2.267(10)
Mn(2)−O(15)	1.905(8)	Mn(4)−O(16)	1.894(7)
Mn(2)−O(1)	1.932(7)	Mn(4)−O(2)	1.920(7)
Mn(2)−O(14)	1.935(8)	Mn(4)−O(17)	1.924(7)
Mn(2)−O(13)	1.935(8)	Mn(4)−O(3)	1.947(7)
Mn(2)−O(6)	2.164(9)	Mn(4)−O(11)	2.134(8)
Mn(2)−O(8)	2.183(8)	Mn(4)−O(7)	2.173(9)
Mn(3)−O(12)	1.867(8)		

O(2)−Mn(1)−O(1)	86.2(3)	O(1)−Mn(3)−O(2)	81.7(3)
O(2)−Mn(1)−O(3)	84.7(3)	O(12)−Mn(3)−O(4)	99.5(3)
O(1)−Mn(1)−O(3)	83.0(3)	O(13)−Mn(3)−O(4)	93.9(3)
O(2)−Mn(1)−O(5)	92.5(3)	O(1)−Mn(3)−O(4)	88.8(3)
O(1)−Mn(1)−O(5)	92.7(3)	O(2)−Mn(3)−O(4)	86.3(3)
O(3)−Mn(1)−O(5)	175.0(3)	O(12)−Mn(3)−O(7)	99.2(3)
O(2)−Mn(1)−O(9)	177.3(4)	O(13)−Mn(3)−O(7)	80.3(3)
O(1)−Mn(1)−O(9)	96.5(3)	O(1)−Mn(3)−O(7)	96.1(3)
O(3)−Mn(1)−O(9)	95.9(3)	O(2)−Mn(3)−O(7)	75.8(3)
O(5)−Mn(1)−O(9)	87.1(3)	O(4)−Mn(3)−O(7)	160.5(3)
O(2)−Mn(1)−O(10)	93.6(3)	O(16)−Mn(4)−O(2)	171.3(3)
O(1)−Mn(1)−O(10)	178.2(3)	O(16)−Mn(4)−O(17)	92.4(3)
O(3)−Mn(1)−O(10)	95.2(3)	O(2)−Mn(4)−O(17)	95.6(3)
O(5)−Mn(1)−O(10)	89.0(3)	O(16)−Mn(4)−O(3)	92.0(3)
O(9)−Mn(1)−O(10)	83.7(3)	O(2)−Mn(4)−O(3)	80.1(3)
O(15)−Mn(2)−O(1)	172.7(4)	O(17)−Mn(4)−O(3)	174.7(3)
O(15)−Mn(2)−O(14)	93.2(4)	O(16)−Mn(4)−O(11)	90.2(3)
O(1)−Mn(2)−O(14)	94.0(3)	O(2)−Mn(4)−O(11)	93.4(3)
O(15)−Mn(2)−O(3)	93.7(3)	O(17)−Mn(4)−O(11)	88.5(3)
O(1)−Mn(2)−O(3)	79.0(3)	O(3)−Mn(4)−O(11)	88.6(3)
O(14)−Mn(2)−O(3)	170.6(3)	O(16)−Mn(4)−O(7)	97.8(3)
O(15)−Mn(2)−O(6)	81.5(4)	O(2)−Mn(4)−O(7)	78.5(3)
O(1)−Mn(2)−O(6)	100.1(4)	O(17)−Mn(4)−O(7)	91.9(3)
O(14)−Mn(2)−O(6)	83.9(4)	O(3)−Mn(4)−O(7)	90.4(3)
O(3)−Mn(2)−O(6)	103.3(3)	O(11)−Mn(4)−O(7)	171.9(3)
O(15)−Mn(2)−O(8)	85.6(4)	Mn(1)−O(1)−Mn(3)	95.1(3)
O(1)−Mn(2)−O(8)	94.2(3)	Mn(1)−O(1)−Mn(2)	95.4(3)
O(14)−Mn(2)−O(8)	84.8(3)	Mn(3)−O(1)−Mn(2)	116.9(4)
O(3)−Mn(2)−O(8)	89.5(3)	Mn(1)−O(2)−Mn(4)	95.8(3)
O(6)−Mn(2)−O(8)	162.3(4)	Mn(1)−O(2)−Mn(3)	94.7(3)
O(12)−Mn(3)−O(13)	90.8(3)	Mn(4)−O(2)−Mn(3)	111.7(4)
O(12)−Mn(3)−O(1)	92.0(3)	Mn(1)−O(3)−Mn(2)	95.2(3)
O(13)−Mn(3)−O(1)	175.7(3)	Mn(1)−O(3)−Mn(4)	94.1(3)
O(12)−Mn(3)−O(2)	171.4(3)	Mn(2)−O(3)−Mn(4)	124.2(4)
O(13)−Mn(3)−O(2)	95.1(3)	Mn(4)−O(7)−Mn(3)	92.1(4)

In contrast, the $Mn^{III}\cdots Mn^{IV}$ separations are much shorter at 2.780(2)−2.802(3) Å.The Mn^{III} ions Mn(2−4) are Jahn−Teller (JT) distorted, as expected for a high-spin d^4 ion in near-octahedral geometry, and the μ_3-$PhCO_2^-$ group occupies positions on all three JT elongation axes (which again avoid O^{2-} ions). Three μ-$PhCO_2^-$ groups bridging each Mn^{III}/Mn^{IV} pair and a chelating dbm^- group on each Mn^{III} complete ligation to the metals. The molecule has virtual C_s symmetry with the mirror plane passing through Mn(1), Mn(2), and O(2).

Complex **12** also crystallizes in monoclinic space group $P2_1/n$ with no crystallographically imposed symmetry on the Mn_4 molecule. The structure is very similar to that of **11** except that a μ_3-$MeCO_2^-$ group now bridges the three Mn^{III} ions with only O(8). This η^1:μ_3-bridging mode leaves O(73) uncoordinated. The molecule is consequently more symmetric, with virtual C_{3v} symmetry if free rotation about O(8)−C(72) is assumed. The $Mn^{III}\cdots Mn^{III}$ separations are now in a much narrower range of 3.195(1)−3.213(1) Å, although the three Mn^{III}−O(8) bonds show some small asymmetry, with Mn(4)−O(8) (2.320(3) Å) being slightly longer than the others (2.281(3) and 2.297(4) Å). The $[Mn_4O_3(\mu_3\text{-}O_2CR)]$ cores of **11** and **12** are conveniently compared in Figure 8, where it can be seen that the $[Mn_4O_3]$ positions are nearly superimposable.

Table 5. Selected Interatomic Distances (Å) and Angles (deg) for $[Mn_4O_3(O_2CMe)_4(dbm)_3]$ (**12**)

Mn(1)···Mn(2)	2.8113(10)	Mn(2)−O(25)	1.914(3)
Mn(1)···Mn(3)	2.7910(11)	Mn(3)−O(5)	1.935(3)
Mn(1)···Mn(4)	2.7941(11)	Mn(3)−O(6)	1.924(3)
Mn(1)−O(5)	1.866(3)	Mn(3)−O(8)	2.297(4)
Mn(1)−O(6)	1.860(3)	Mn(3)−O(17)	2.141(3)
Mn(1)−O(7)	1.876(3)	Mn(3)−O(38)	1.926(3)
Mn(1)−O(9)	1.923(3)	Mn(3)−O(42)	1.912(3)
Mn(1)−O(13)	1.961(3)	Mn(4)−O(6)	1.936(3)
Mn(1)−O(19)	1.941(3)	Mn(4)−O(7)	1.914(3)
Mn(2)−O(5)	1.936(3)	Mn(4)−O(8)	2.320(3)
Mn(2)−O(7)	1.954(3)	Mn(4)−O(15)	2.154(3)
Mn(2)−O(8)	2.281(3)	Mn(4)−O(55)	1.913(3)
Mn(2)−O(11)	2.173(3)	Mn(4)−O(59)	1.932(3)
Mn(2)−O(21)	1.918(3)		

O(5)−Mn(1)−O(6)	85.45(14)	O(8)−Mn(3)−O(38)	96.10(14)
O(5)−Mn(1)−O(7)	85.76(14)	O(8)−Mn(3)−O(42)	98.99(14)
O(5)−Mn(1)−O(9)	94.29(14)	O(17)−Mn(3)−O(38)	95.08(14)
O(5)−Mn(1)−O(13)	177.36(14)	O(17)−Mn(3)−O(42)	89.48(14)
O(5)−Mn(1)−O(19)	93.41(15)	O(38)−Mn(3)−O(42)	92.11(14)
O(6)−Mn(1)−O(7)	85.11(14)	O(6)−Mn(4)−O(7)	82.02(13)
O(6)−Mn(1)−O(9)	178.46(14)	O(6)−Mn(4)−O(8)	79.13(13)
O(6)−Mn(1)−O(13)	91.93(14)	O(6)−Mn(4)−O(15)	86.38(13)
O(6)−Mn(1)−O(19)	92.51(15)	O(6)−Mn(4)−O(55)	92.08(14)
O(7)−Mn(1)−O(9)	93.35(14)	O(6)−Mn(4)−O(59)	175.76(14)
O(7)−Mn(1)−O(13)	94.34(14)	O(7)−Mn(4)−O(8)	80.14(13)
O(7)−Mn(1)−O(19)	177.54(15)	O(7)−Mn(4)−O(15)	91.14(13)
O(9)−Mn(1)−O(13)	88.34(14)	O(7)−Mn(4)−O(55)	173.67(15)
O(9)−Mn(1)−O(19)	89.02(14)	O(7)−Mn(4)−O(59)	94.36(14)
O(13)−Mn(1)−O(19)	86.39(14)	O(8)−Mn(4)−O(15)	163.95(13)
O(5)−Mn(2)−O(7)	81.74(13)	O(8)−Mn(4)−O(55)	96.54(13)
O(5)−Mn(2)−O(8)	80.26(13)	O(8)−Mn(4)−O(59)	98.13(13)
O(5)−Mn(2)−O(11)	87.83(13)	O(15)−Mn(4)−O(55)	90.78(14)
O(5)−Mn(2)−O(21)	173.91(14)	O(15)−Mn(4)−O(59)	95.93(14)
O(5)−Mn(2)−O(25)	92.89(14)	O(55)−Mn(4)−O(59)	91.45(14)
O(7)−Mn(2)−O(8)	80.32(13)	Mn(1)−O(5)−Mn(2)	95.35(15)
O(7)−Mn(2)−O(11)	86.48(13)	Mn(1)−O(5)−Mn(3)	94.49(14)
O(7)−Mn(2)−O(21)	92.81(14)	Mn(2)−O(5)−Mn(3)	111.23(16)
O(7)−Mn(2)−O(25)	174.63(14)	Mn(1)−O(6)−Mn(3)	95.02(15)
O(8)−Mn(2)−O(11)	163.32(12)	Mn(1)−O(6)−Mn(4)	94.76(14)
O(8)−Mn(2)−O(21)	96.21(14)	Mn(3)−O(6)−Mn(4)	112.64(15)
O(8)−Mn(2)−O(25)	98.82(13)	Mn(1)−O(7)−Mn(2)	94.43(15)
O(11)−Mn(2)−O(21)	94.57(14)	Mn(1)−O(7)−Mn(4)	95.00(14)
O(11)−Mn(2)−O(25)	93.36(14)	Mn(2)−O(7)−Mn(4)	11.41(16)
O(21)−Mn(2)−O(25)	92.56(14)	Mn(2)−O(8)−Mn(3)	88.49(12)
O(5)−Mn(3)−O(6)	81.84(14)	Mn(2)−O(8)−Mn(4)	87.98(12)
O(5)−Mn(3)−O(8)	79.88(13)	Mn(2)−O(8)−C(72)	122.3(3)
O(5)−Mn(3)−O(17)	90.35(14)	Mn(3)−O(8)−Mn(4)	88.18(11)
O(5)−Mn(3)−O(38)	94.63(14)	Mn(3)−O(8)−C(72)	124.2(3)
O(5)−Mn(3)−O(42)	173.24(15)	Mn(4)−O(8)−C(72)	132.8(3)
O(6)−Mn(3)−O(8)	79.94(13)	Mn(1)−O(9)−C(10)	125.7(3)
O(6)−−Mn(3)−O(17)	88.39(13)	O(8)−C(72)−C(73)	122.8(5)
O(6)−Mn(3)−O(38)	175.08(14)	O(8)−C(72)−C(74)	116.1(4)
O(6)−Mn(3)−O(42)	91.40(14)	O(73)−C(72)−C(74)	121.1(5)
O(8)−Mn(3)−O(17)	165.69(13)		

Complexes **11** and **12** thus possess structures that represent new additions to the near-isostructural family of $[Mn_4O_3X(O_2CMe)_3(dbm)_3]$ (X = Cl, Br) species,[12] the only difference between them being the identity of X. Complex **11** does differ in the bidentate nature of its μ_3-$PhCO_2^-$, which begs the question why. It appears that the origin of the different bridging modes in **11** vs **12** is steric: in Figure 9 are shown space-filling stereoviews down the C_3 rotation axis of the $[Mn_4O_3]$ core (i.e., through the Mn^{IV} ion). The dbm groups form a concave cavity in which resides the μ_3-RCO_2^- group. For the latter to convert to a η^1:μ_3-mode, its Ph ring would have to tilt by ∼60°, but this would be unfavorable due to steric interactions with the dbm groups. In contrast, the smaller $MeCO_2^-$ group can bind η^1:μ_3 without steric problems. It could, of course, also bind like the $PhCO_2^-$ group in **11**, and this suggests that, other things

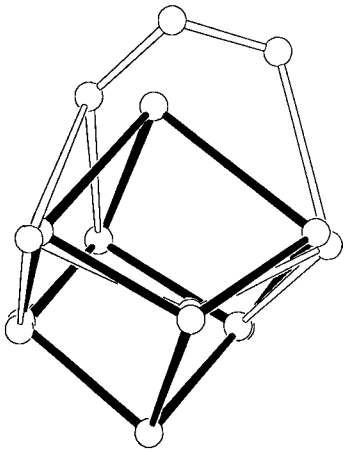

Figure 8. Comparison of the cores of **11** (open lines) and **12** (black lines) showing the near superimposability of the $[Mn_4(\mu_3\text{-}O)_3]$ portions. For **11**, the $PhCO_2^-$ phenyl group is omitted, while for **12** only the metal-bound $MeCO_2^-$ O atom is shown.

being equal, the η^1:μ_3-binding mode for a RCO_2^- group is the favored one.

Magnetochemistry of Complexes 11 and 12. Variable-temperature magnetic susceptibility data (χ_M) were collected on powdered samples of **11** and **12** in the 2.00−320 K range.

For **11**, the effective magnetic moment (μ_{eff}) per Mn_4 gradually increases from 7.81 μ_B at 320 K to a maximum of 9.24 μ_B at 20.0 K and then decreases slightly to 8.63 μ_B at 5.01 K (Figure 10). These correspond to $\chi_M T$ values of 7.62, 10.67, and 9.31 cm^3 K mol^{-1} at three temperatures. The data thus suggest a relatively high ground state spin value, and the maximum μ_{eff} value of 9.24 μ_B at 20.0 K is comparable with the spin-only ($g = 2.00$) value of 9.95 μ_B expected for a $S = {}^9/_2$ state.

In order to fit the experimental data, an appropriate theoretical χ_M vs T and μ_{eff} vs T expression for **11** was sought. The C_s symmetry of the core requires four exchange parameters (J), as shown in Figure 11. The Heisenberg spin Hamiltonian describing the pairwise interactions is given in eq 8. A full-matrix

$$\hat{H} = -2J_{34}(\hat{S}_1\hat{S}_3 + \hat{S}_1\hat{S}_4) - 2J'_{34}\hat{S}_1\hat{S}_2 - 2J_{33}(\hat{S}_2\hat{S}_4 + \hat{S}_3\hat{S}_4) - 2J'_{33}\hat{S}_3\hat{S}_4 \quad (8)$$

diagonalization approach for obtaining the eigenvalues of this spin Hamiltonian would require diagonalization of a 500 × 500 matrix. Unfortunately, the more convenient equivalent operator approach, based on the Kambe vector coupling method,[23] is not possible for this C_s symmetry system. However, a very reasonable simplifying approximation is possible by taking $J_{34} = J_{34}'$: these interactions are likely very similar since both pathways involve very similar $[Mn_2(\mu\text{-}O^{2-})_2]^{3+}$ rhombs (vide supra). The spin Hamiltonian now becomes that given in eq 9, for which the Kambe method is applicable. Using the substitu-

$$\hat{H} = -2J_{34}(\hat{S}_1\hat{S}_2 + \hat{S}_1\hat{S}_3 + \hat{S}_1\hat{S}_4) - 2J_{33}(\hat{S}_2\hat{S}_4 + \hat{S}_3\hat{S}_4) - 2J'_{33}\hat{S}_3\hat{S}_4 \quad (9)$$

tions $\hat{S}_A = \hat{S}_3 + \hat{S}_4$, $\hat{S}_B = \hat{S}_A + \hat{S}_2$, and $\hat{S}_T = \hat{S}_B + \hat{S}_1$, where S_T is the spin of the complete Mn_4 unit, the spin Hamiltonian of eq 9 can be converted to the equivalent one in eq 10. The

$$\hat{H} = -J_{34}[\hat{S}_T{}^2 - \hat{S}_B{}^2 - \hat{S}_1{}^2] - J_{33}[\hat{S}_B{}^2 - \hat{S}_A{}^2 - \hat{S}_2{}^2] - J'_{33}[\hat{S}_A{}^2 - \hat{S}_3{}^2 - \hat{S}_4{}^2] \quad (10)$$

eigenvalues for this Hamiltonian are given in eq 11, where constant terms contributing to all states have been omitted. For

$$E(S_T) = -J[S_T(S_T + 1) - S_B(S_B + 1)] - J_{33}[S_B(S_B + 1) - S_A(S_A + 1)] - J'_{33}[S_A(S_A + 1)] \quad (11)$$

complex **11**, $S_1 = {}^3/_2$, $S_2 = S_3 = S_4 = 2$, and the overall degeneracy of the spin system is 500, made up of 70 individual spin states ranging from $S_T = {}^1/_2$ to ${}^{15}/_2$.

A theoretical χ_M vs T expression for complex **11** was derived using the Van Vleck equation[24] and eq 11, and this expression, in the form of μ_{eff} vs T, was used to fit the experimental data: only data at 20.0 K and above were employed since the decrease below 20.0 K is likely due to a combination of Zeeman effects, zero-field splitting (ZFS), and intermolecular exchange interactions, none of which is incorporated into the fitting model. An excellent fit was obtained (solid line in Figure 10) having fitting parameters $J_{34} = -28.5$ cm^{-1}, $J_{33} = +2.8$ cm^{-1}, $J'_{33} = +2.1$ cm^{-1}, and $g = 1.85$, with temperature independent paramagnetism (TIP) held constant at 800 × 10^{-6} cm^3 mol^{-1}. These parameters indicate a $S_T = {}^9/_2$ ground state for **11**, with a $S_T = {}^7/_2$ first excited state.

For complex **12**, the μ_{eff} per Mn_4 gradually decreases from 8.37 μ_B at 320 K to a plateau of 9.64 μ_B at 20.0−40.0 K, and then decreases to 6.93 μ_B at 2.00 K (Figure 12). These correspond to $\chi_M T$ values of 8.76, 11.62, and 6.00 cm^3 K mol^{-1} at these three temperatures. The experimental data at temperatures ≥20.0 K were fit to the theoretical expression derived previously[12a] for a C_{3v} symmetry Mn_4 trigonal pyramid with exchange parameters J_{34} and J_{33} for the Mn^{III}/Mn^{IV} and Mn^{III}/Mn^{III} interactions, respectively. This is also that obtained from Figure 11 and eqs 8−11 by putting $J_{34} = J'_{34}$ and $J_{33} = J'_{33}$. The fit, shown as a solid line in Figure 12, has $J_{34} = -33.9$ cm^{-1}, $J_{33} = +5.4$ cm^{-1}, and $g = 1.94$, with TIP held constant at 800 × 10^{-6} cm^3 mol^{-1}. This fit again indicates a $S_T = {}^9/_2$ ground state and a $S_T = {}^7/_2$ first excited state.

In order to confirm the $S_T = {}^9/_2$ ground states for **11** and **12**, magnetization (M) data were collected in the 2.00−30.0 K range in magnetic fields of 0.50−50 kG. These data, shown in Figures 13 and 14 as reduced magnetization ($M/N\mu_B$) vs H/T plots, were fit by diagonalization of the spin Hamiltonian matrix incorporating axial ZFS (DS_Z^2) and Zeeman interactions, and assuming only the ground state to be occupied at these temperatures. In both cases, good fits were obtained (shown as solid lines in Figures 13 and 14) with fitting parameters, in the format **11**/**12**, of $S_T = {}^9/_2$ (for both), $g = 2.01/1.96$, and $D = -0.58/-0.47$ cm^{-1}.

The S_T and J values obtained for **11** and **12** are compared in Table 6 with those obtained previously for $[Mn_4O_3X(O_2CMe)_3(dbm)_3]$ complexes with the C_{3v}-symmetry $[Mn_4(\mu_3\text{-}O)_3(\mu_3\text{-}X)]^{6+}$ core.[12] As can be seen, the four complexes have similar properties: in all cases, the J_{34} and J_{33} parameters are antiferromagnetic and ferromagnetic, respectively, and although there is some variation in absolute magnitude, they are all in the −30 ± 3 cm^{-1} and 5 ± 3 cm^{-1} ranges, respectively. This is as expected from their very similar structural parameters, and it appears that the additional structural perturbations present as a result of the η^2-benzoate group in **11** have little consequence to the resultant magnetic properties. This is consistent with the conclusion that the dominant pathways for the exchange interactions between Mn^{III}/Mn^{IV} pairs *and* between Mn^{III}/Mn^{III}

(23) Kambe, K. *J. Phys. Soc. Jpn.* **1950**, *5*, 48.
(24) Van Vleck, J. H. *The Theory of Electric and Magnetic Susceptibilities*; Oxford University Press: London, 1932.

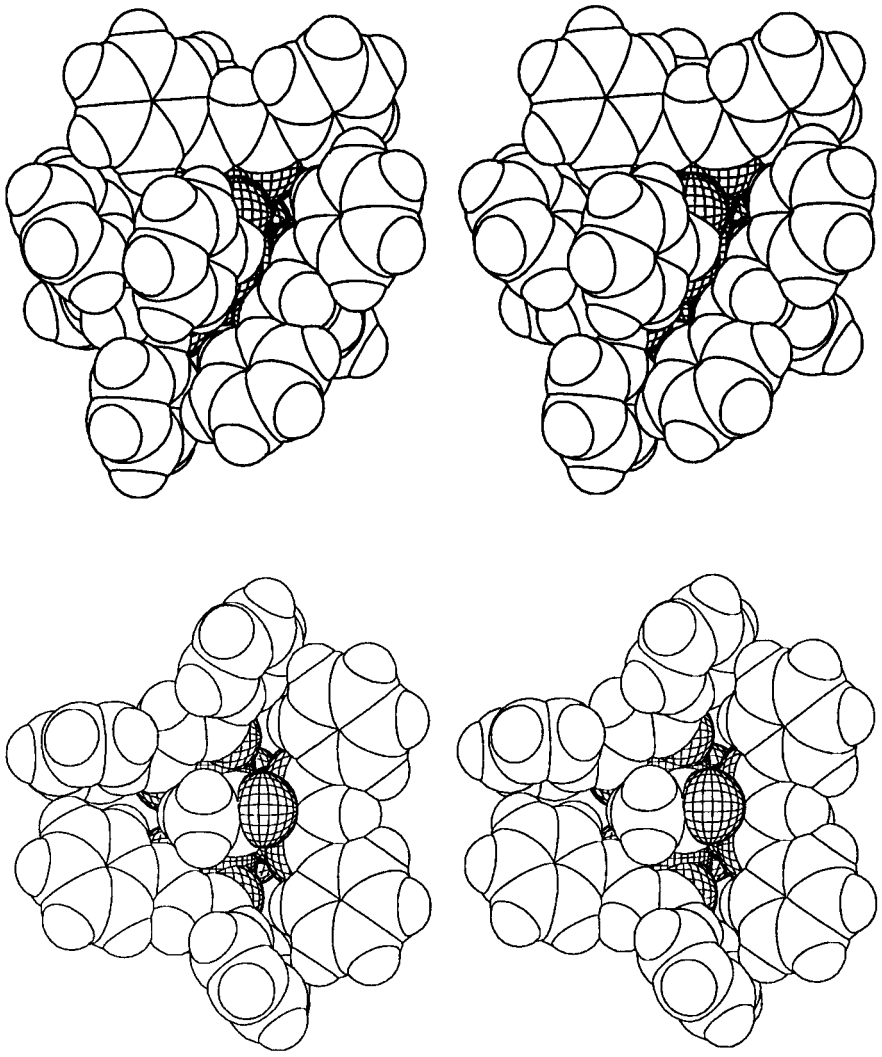

Figure 9. Space-filling stereoviews approximately along the C_3 virtual axes of **11** (top) and **12** (bottom) showing the μ_3-O_2CR group in a concave cavity formed by the dbm groups.

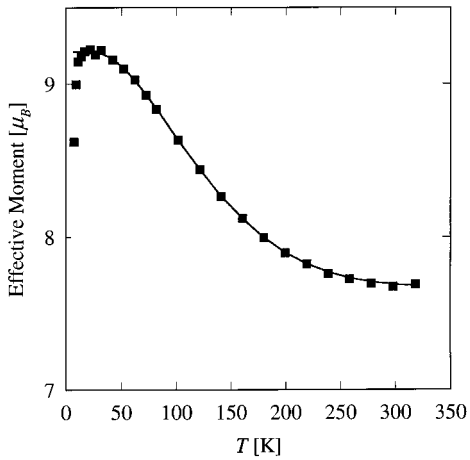

Figure 10. Plot of effective magnetic moment (μ_{eff}) vs temperature for $[Mn_4O_3(O_2CPh)_4(dbm)_3]$ (**11**). The solid line is a fit of the data to the appropriate theoretical expression; see the text for the fitting parameters.

pairs are the oxide bridges. Also compared in Table 6 are the energy separations between the $S_T = {}^9/_2$ ground states and the $S_T = {}^7/_2$ first excited states, and the D values obtained from the $M/N\mu_B$ vs H/T fits. In all cases, the $S_T = {}^7/_2$ first excited state is at relatively high energy, and the complexes thus possess well-isolated ground states. Note, however, that this separation

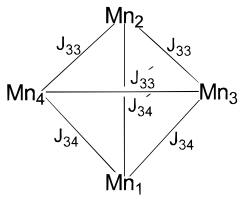

Figure 11. The exchange interactions in complex **11** with C_s symmetry. The Mn numbering corresponds to that in Figure 6: $Mn_1 = Mn^{IV}$, $Mn_2 = Mn_3 = Mn_4 = Mn^{III}$. J_{33} and J_{34} refer to Mn^{III}/Mn^{III} and Mn^{III}/Mn^{IV} interactions, respectively.

for **11** is the smallest among these compounds as a result of its weaker J_{33} and J_{33}' interactions compared with J_{33} for the μ_3,η^1-X^- complexes. Similarly, the D values of the four complexes are of comparable magnitude, with complex **11** having the greatest absolute magnitude. Note that the absolute magnitudes of the D values are slightly larger than we reported previously;[4c] for complex **12**, we previously reported that $D = -0.32$ cm^{-1}. The present values in Table 6 are considered more reliable because they have been obtained with a matrix diagonalization theoretical approach that calculates a full powder average, whereas the earlier procedure did not involve a powder average. Also note that fitting of magnetization data generally yields two minima, one with $D > 0$ and one with $D < 0$, usually giving comparable fits of the data.[4c] However, we consider only the D

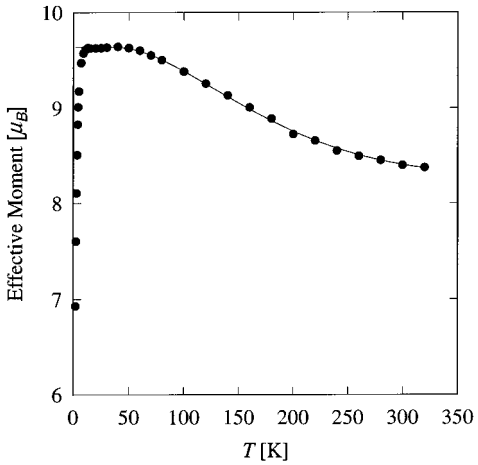

Figure 12. Plot of effective magnetic moment (μ_{eff}) vs temperature for $[Mn_4O_3(O_2CMe)_4(dbm)_3]$ (**12**). The solid line is a fit of the data to the appropriate theoretical expression; see the text for the fitting parameters.

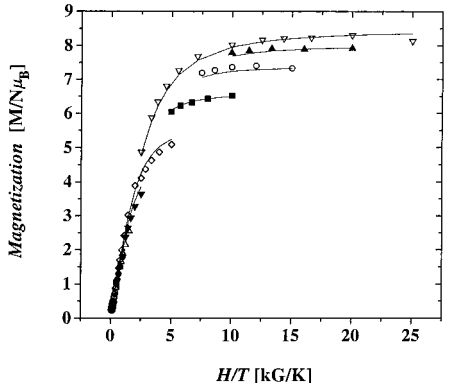

Figure 13. Plot of reduced magnetization ($M/N\mu_B$) vs H/T for complex **11** at 0.50 (●), 1.00 (□), 3.00 (△), 5.00 (▼), 10.0 (◇), 20.0 (■), 30.0 (○), 40.0 (▲), and 50.0 kG (▽). The solid lines result from a least-squares fit of the data; see the text for the fitting procedure and the fitting parameters.

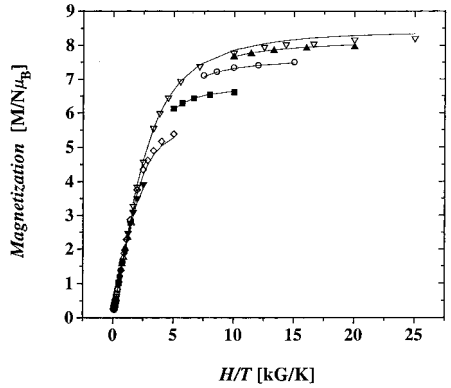

Figure 14. Plot of reduced magnetization ($M/N\mu_B$) vs H/T for complex **12** at 0.50 (●), 1.00 (□), 3.00 (△), 5.00 (▼), 10.0 (◇), 20.0 (■), 30.0 (○), 40.0 (▲), and 50.0 kG (▽). The solid lines result from a least-squares fit of the data; see the text for the fitting procedure and the fitting parameters.

< 0 fits in the present work because previous studies of the temperature dependencies of high-field EPR signals have shown unequivocally that $D < 0$ for these $[Mn_4O_3X(O_2CMe)_3(dbm)_3]$ complexes.[4b]

Discussion

A variety of Mn carboxylate species has been obtained by a combination of synthetic methods. The dbm^- anion continues to prove a valuable chelate in the stabilization of tetranuclear species, as well as other nuclearities, and this has allowed reactivity characteristics of certain species to be assessed. In the present work, dbm^- has been used to prepare new $[Mn_4O_2]^{8+}$-containing complexes **6**−**10** whose electrochemical signatures suggest a quasi-reversible oxidation. The consequences of this oxidation have been explored, and the products of the CPE experiments, complexes **11** and **12**, have been found to have distinctly different cores from the starting materials, with an increased O^{2-}:Mn ratio. This and the reaction conditions and yields of **11** and **12** suggest that these final products are forming by reaction of the electrochemically oxidized starting materials with H_2O molecules in the solvent. The overall transformations to give **11** and **12** are summarized in eqs 6 and 7, respectively. We envisage the sequence of events to, e.g., complex **11** to involve an initial oxidation of the $[Mn_4O_2(O_2CPh)_7(dbm)_2]^-$ anion of **10** to give $[Mn_4O_2(O_2CPh)_7(dbm)_2]$ (eq 12), which is then attacked by an H_2O molecule. Although

$$[Mn_4O_2(O_2CPh)_7(dbm)_2]^- \xrightarrow{-e^-} [Mn_4O_2(O_2CPh)_7(dbm)_2] \quad (12)$$

the identity of transient intermediates is not known, we suggest that it may involve species in which the water has bound, has been deprotonated, and is bridging a Mn^{III}/Mn^{IV} pair as a OH^-, the displaced $PhCO_2^-$ acting as the H^+ acceptor (eq 13); the core transformation is depicted in Scheme 2. The conversion

$$[Mn_4O_2(O_2CPh)_7(dbm)_2] + H_2O \rightarrow [Mn_4O_2(OH)(O_2CPh)_6(dbm)_2] + PhCO_2H \quad (13)$$

of this $[Mn_4O_2(OH)]$ core to that of final product **11** now requires deprotonation of the OH^- and its conversion to a μ_3-O^{2-} (Scheme 2) concomitant with attachment of a third dbm^- group, with the displaced $PhCO_2^-$ groups again acting as Brønsted bases for the OH^- *and* dbmH deprotonations (eqs 6 and 7). Note that Scheme 2 is consistent with the structural

Table 6. Comparison of Fitting Parameters for $[Mn_4O_3X(O_2CR)_3(dbm)_3]$ Complexes

	X			
param[a]	O_2CPh (**11**)	O_2CMe (**12**)	Cl	Br
J_{34}, cm^{-1}	−28.5	−33.9	−28.4	−30.1
J_{33}, cm^{-1}	+2.8	+5.4	+8.3	+7.4
J'_{33}, cm^{-1}	+2.1			
ground S_T	$^9/_2$	$^9/_2$	$^9/_2$	$^9/_2$
$E(S_T = {}^7/_2)$,[b] cm^{-1}	114	167	185	179
g	2.01	1.96	2.00	2.01
D, cm^{-1}	−0.58	−0.47	−0.35	−0.50
ref	*c*	*c*	*d*	*e*

[a] $J_{34} = J(Mn^{III}/Mn^{IV})$; $J_{33} = J(Mn^{III}/Mn^{III})$. [b] Energy of the $S_T = {}^7/_2$ first excited state above the ground state. [c] This work. [d] Ref 4c. [e] Redetermined with a negative D (see text).

Scheme 2

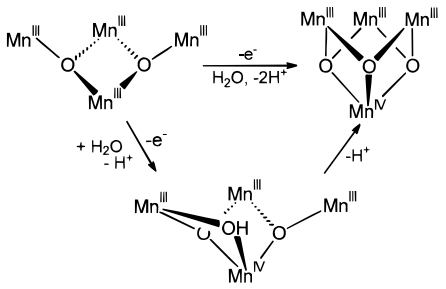

relationship between the $[Mn_4O_2]$ and $[Mn_4O_3]$ cores, i.e., the latter is a "closed-up" version of the former caused by the presence of a third μ_3-O^{2-} ion. Also note that the spontaneous incorporation of an extra O^{2-} ion on oxidation of the $[Mn_4O_2]$ core is consistent with the general trend that increasing average oxidation state favors an increase in the proportion of hard O^{2-} ions.[25] The MnO_4^- ion lies at one extreme of this relationship. The spontaneous incorporation of a third O^{2-} ion in **11** and **12** is thus consistent with the average oxidation state increase from +3.00 to +3.25. Alternatively, one can describe this as the third O^{2-} ion helping to stabilize the higher oxidation state species.[12a]

From a biological viewpoint, the results described in this paper offer some food for thought. The coupled oxidation/oxide incorporation seen in going from, for example, $[Mn_4O_2]$ complex **10** to $[Mn_4O_3]$ complex **11** could be considered a model system for the progressive oxidation/substrate activation processes in the native WOC, i.e., H_2O-derived O^{2-} ions are stabilizing the increasing WOC S_n oxidation level, and, inversely, of course, the increasing WOC S_n oxidation level is stabilizing activated/deprotonated forms of H_2O in preparation for their oxidative coupling to O_2.

The above discussion can be extended one step further when our recently reported[26] observation is noted that complex **12** will react with H_2O to give $[Mn_4O_3(OH)(O_2CMe)_3(dbm)_3]$, a μ_3-OH^- replacing the μ_3-O_2CMe^-. In effect, this and the conversion of **6** to **12** provide the demonstration of the sequence of eq 14 that represents the activation of two H_2O molecules

$$[Mn_4O_2] \xrightarrow[H_2O]{-e^-} [Mn_4O_3] \xrightarrow[H_2O]{} [Mn_4O_3(OH)] \qquad (14)$$

by binding to Lewis acidic Mn^{n+} centers and partial or complete deprotonation. Fuller details will be provided in a subsequent paper on the hydrolysis of **12**. The $[Mn_4O_2]$ and $[Mn_4O_3]$ complexes are not exact structural models of the WOC on the basis of, for example, EXAFS data[27] and ground state spin differences; however, the oxidation-driven chemistry they are exhibiting may nevertheless be providing important insights into the means by which H_2O molecules are bound and activated to oxidation to O_2 in photosynthesis, whatever the precise structure of the native WOC may be.

Acknowledgment. This work was supported by NIH Grant GM 39083 to G.C. and NSF Grant CHE 9727312 to D.N.H.

Supporting Information Available: Tables of crystallographic data, structure refinement details, atomic coordinates, interatomic distances and angles, anisotropic thermal parameters, and calculated hydrogen parameters. This material is available free of charge via the Internet at http://pubs.acs.org.

IC991068M

(25) Christou, G.; Vincent, J. B. In *Metal Clusters in Proteins;* ACS Symp. Ser. 372; Que, L., Ed.; American Chemical Society, 1988; Chapter 12, pp 238−255.

(26) Aromí, G.; Wemple, M. W.; Aubin, S. M. J.; Folting, K.; Hendrickson, D. N.; Christou, G. *J. Am. Chem. Soc.* **1998**, *120*, 5850.

(27) Cinco, R. M.; Rompel, A.; Visser, H.; Aromí, G.; Christou, G.; Sauer, K.; Yachandra, V. K.; Klein, M. P. *Inorg. Chem.*, in press.